

1 **Effects of ^{238}U variability and physical transport on water column**

2 **^{234}Th downward fluxes in the coastal upwelling system off Peru**

3

4 Ruifang C. Xie^{1*}, Frédéric A. C. Le Moigne², Insa Rapp¹, Jan Lüdke¹, Beat Gasser³, Marcus

5 Dengler¹, Volker Liebetrau¹, Eric P. Achterberg¹

6

7 ¹GEOMAR Helmholtz Center for Ocean Research Kiel, Wischhofstrasse 1-3, 24148 Kiel,

8 Germany

9 ²Mediterranean Institute of Oceanography (UM 110, MIO), CNRS, IRD, Aix Marseille

10 Université, Marseille, France

11 ³IAEA Environment Laboratories, 4 Quai Antoine 1er, 98000 Monaco

12 Monaco

13

14 * corresponding author: rxie@geomar.de

15 **Abstract**

16 The eastern boundary region of the southeastern Pacific Ocean hosts one of the world's most
17 dynamic and productive upwelling systems with an associated oxygen minimum zone (OMZ).
18 The variability in downward export fluxes in this region, with strongly varying surface
19 productivity, upwelling intensities and water column oxygen content, is however poorly
20 understood. Thorium-234 (^{234}Th) is a powerful tracer to study the dynamics of export fluxes
21 of carbon and other elements, yet intense advection and diffusion in nearshore environments
22 impact the assessment of depth-integrated ^{234}Th fluxes when not properly evaluated. Here we
23 use VmADCP current velocities, satellite wind speed and *in situ* microstructure measurements
24 to determine the magnitude of advective and diffusive fluxes over the entire ^{234}Th flux budget
25 at 25 stations from 11°S to 16°S in the Peruvian OMZ. Contrary to findings along the
26 GEOTRACES P16 eastern section, our results showed that weak surface wind speed during
27 our cruises induced low upwelling rates and minimal upwelled ^{234}Th fluxes, whereas vertical
28 diffusive ^{234}Th fluxes were important only at a few shallow shelf stations. Horizontal
29 advective and diffusive ^{234}Th fluxes were negligible because of small alongshore ^{234}Th
30 gradients. Our data indicated a poor correlation between seawater ^{238}U activity and salinity.
31 Assuming a linear relationship between the two would lead to significant underestimations of
32 the total ^{234}Th flux by up to 40% in our study. Proper evaluation of both physical transport
33 and variability in ^{238}U activity is thus crucial in coastal ^{234}Th flux studies. Finally, we showed
34 large temporal variations on ^{234}Th residence times across the Peruvian upwelling zone, and
35 cautioned future carbon export studies to take these temporal variabilities into consideration
36 while evaluating carbon export efficiency.

37 **Keywords:** eastern tropical South Pacific, ^{234}Th tracer, uranium-salinity correlation, physical
38 processes, residence time

39 1. Introduction

40 Isotopes of thorium (Th) are widely used as tracers for particle cycling in the oceans
41 (Waples et al., 2006). In particular, ^{234}Th has been extensively used to trace particle dynamics
42 and export fluxes in the upper ocean, and to quantify the marine budgets of important macro-
43 and micronutrients such as carbon (C), nitrogen (N), phosphorus (P) and iron (Fe) (Bhat et al.,
44 1968; Buesseler et al., 1992; Coale and Bruland, 1987; Lee et al., 1998; Le Moigne et al.,
45 2013; Cochran and Masqué, 2003; Van Der Loeff et al., 2006; Black et al., 2019). ^{234}Th has a
46 relatively short half-life ($\tau_{1/2} = 24.1$ days) that allows studies of biological and physical
47 processes occurring on timescales of days to weeks. Unlike its radioactive parent uranium-238
48 (^{238}U , $\tau_{1/2} = 4.47$ Ga) that is soluble in seawater, ^{234}Th is highly particle reactive with a
49 particle-water partition coefficient of 10^3 to 10^8 (Santschi et al., 2006 and references therein)
50 and thus strongly scavenged by particles (Bhat et al., 1968). Generally, a deficit of ^{234}Th
51 relative to ^{238}U is observed in the surface ocean and reflects net removal of ^{234}Th due to
52 particle sinking, whereas secular equilibrium between ^{234}Th and ^{238}U is observed for
53 intermediate and deep waters. Integrating this surface ^{234}Th deficit with depth yields the
54 sinking flux of ^{234}Th and, if elemental: ^{234}Th ratios are known, the sinking flux of elements
55 such as C, N, P, and trace metals (Bhat et al., 1968; Buesseler et al., 1998; Buesseler et al.,
56 1992; Coale and Bruland, 1987; Weinstein and Moran, 2005; Buesseler et al., 2006; Owens et
57 al., 2015; Black et al., 2019; Puigcorbé et al., 2020).

58 Various ^{234}Th models have been put forward to study adsorption/desorption,
59 aggregation and export, but single box models that assume negligible ^{234}Th fluxes due to
60 physical transport are commonly used to calculate oceanic ^{234}Th -derived particle fluxes (see
61 detailed review by Savoye et al., 2006). This assumption is typically appropriate in open
62 ocean settings where ^{234}Th fluxes due to advection and diffusion are small relative to the
63 downward fluxes of ^{234}Th associated with particle sinking. However, in upwelling regions

64 such as the equatorial Pacific and coastal systems, advective and diffusive ^{234}Th fluxes may
65 become increasingly important (e.g., Bacon et al., 1996; Buesseler et al., 1998; Buesseler et
66 al., 1995; Dunne and Murray, 1999). For example, in the equatorial Pacific, strong upwelling
67 post El-Niño could account for ~50% of the total ^{234}Th fluxes (Bacon et al., 1996; Buesseler
68 et al., 1995). Ignoring the upwelling term could thus lead to an underestimation of ^{234}Th
69 fluxes by a factor of 2. Conversely, horizontal diffusion carrying recently upwelled, ^{234}Th -
70 replete waters has been shown to balance the upwelled ^{234}Th fluxes in the central equatorial
71 Pacific (Dunne and Murray, 1999). To the contrary, advective and diffusive ^{234}Th fluxes were
72 minimal off the Crozet Islands in the Southern Ocean due to limited horizontal ^{234}Th
73 gradients, long residence time of water masses, and low upwelling rates and diffusivities
74 (Morris et al., 2007).

75 The dynamic nature of coastal processes requires that physical terms be included in
76 ^{234}Th flux calculation whenever possible. Accurate measurements of current velocities and
77 diffusivities are however challenging and thus direct observations of the effects of physical
78 processes on ^{234}Th distributions in coastal regions are scarce. Limited studies have
79 incorporated advection and diffusion in the nearshore zones of the Arabian Sea (Buesseler et
80 al., 1998), Gulf of Maine (Gustafsson et al., 1998; Benitez-Nelson et al., 2000), the South
81 China Sea (Cai et al., 2008) and Peruvian oxygen minimum zone (OMZ) (Black et al., 2018).
82 In the Arabian Sea, coastal upwelling during the southwest monsoon season could account for
83 over 50% of the total ^{234}Th flux (Buesseler et al., 1998). Horizontal advection has been shown
84 to be substantial in the Inner Cosco Bay of the Gulf of Maine (Gustafsson et al., 1998),
85 whereas offshore advection and diffusion are only important in late summer (Benitez-Nelson
86 et al., 2000). Therefore, the importance of physical processes on the ^{234}Th flux estimate is
87 highly dependent on the seasonal and spatial variability of the current velocities, diffusivities
88 and ^{234}Th gradients. In terms of the Peruvian OMZ, Black et al. (2018) showed that coastal

89 upwelling accounts for >50% of total ^{234}Th fluxes at 12°S; however, how upwelling ^{234}Th
90 fluxes vary seasonally and spatially in this region is unclear.

91 Another uncertainty in ^{234}Th flux calculations in such region stems from variations on
92 dissolved ^{238}U activities. Generally speaking, U behaves conservatively under open ocean
93 oxic conditions and is linearly correlated with salinity (Chen et al., 1986; Ku et al., 1977;
94 Owens et al., 2011). However, numerous studies have shown that such correlation breaks
95 down in various marine environments including the tropical Atlantic (Owens et al., 2011),
96 Mediterranean Sea (Schmidt and Reys, 1991), and Arabian Sea (Rengarajan et al., 2003).
97 Although it is generally accepted that deviations from the linear ^{238}U -S correlation will lead to
98 differences in the final calculated ^{234}Th fluxes, there is currently little knowledge on how
99 significant these differences could be.

100 In this study, we report vertical profiles of ^{234}Th and ^{238}U along four transects
101 perpendicular to the coastline of Peru (i.e. shelf-offshore transects). We evaluate the ^{238}U -S
102 correlation in low-oxygen waters and how deviations from this correlation impact final ^{234}Th
103 flux estimates. We also assess the spatial and temporal importance of advection and diffusion
104 on ^{234}Th flux estimates.

105

106 **2. Sampling and methods**

107 2.1 Seawater sampling and analysis

108 Seawater samples were collected at 25 stations along 4 shelf-offshore transects
109 between 11°S and 16°S in the Peruvian OMZ during two cruises M136 and M138 on board
110 the RV Meteor (Figure 1). Cruise M136 took place in austral autumn (April 11 to May 3,
111 2017) along two main transects at 12°S and 14°S (Dengler and Sommer, 2017). Two stations
112 from M136 (stations 458 and 495) were reoccupied within a week (repeat stations 508 and

113 516, respectively) to evaluate the steady-state assumption in the ^{234}Th flux calculation. The
114 surface sample of the repeat station 508 (reoccupied 4.5 days after station 458) was missing so
115 only results from repeat stations 495 and 516 (occupation interval 1.5 days) were compared
116 and discussed in terms of the non-steady state model (section 3.3). ^{234}Th sampling during
117 cruise M138 was carried out in austral winter (June 1 to July 4, 2017) and focused on four
118 shelf-offshore transects at 11°S , 12°S , 14°S and 16°S .

119 At each station, a stainless-steel rosette with Niskin bottles (Ocean Test Equipment[®])
120 was deployed for sampling of total ^{234}Th in unfiltered seawater and dissolved ^{238}U ($0.2\ \mu\text{m}$
121 pore size, Acropak[®] polycarbonate membrane). High vertical resolution sampling was
122 performed in the upper 200 m where most of the biological activity occurs; additional depths
123 were sampled down to 600 m, or 50 m above the seafloor. Deep seawater at 1000 m, 1500 m,
124 and 2000 m was sampled at three stations to determine the absolute β counting efficiency.
125 Salinity, temperature, oxygen concentrations and fluorescence data (Table S1) were derived
126 from the sensors (Seabird Electronics[®] 9plus system) mounted on the CTD frame (Krahmann,
127 2018; Lüdke et al., in review 2020).

128 Sample collection and subsequent chemical processing and analysis for total ^{234}Th
129 followed protocols by Pike et al. (2005) and SCOR Working Group RiO5 cookbook
130 (<https://cmer.who.edu/>). Briefly, a ^{230}Th yield tracer (1 dpm) was added to each sample (4 L)
131 before Th was extracted with MnO_2 precipitates. Precipitates were filtered onto 25 mm quartz
132 microfiber filters (Whatman[®] QMA, $2.2\ \mu\text{m}$ nominal pore size) and dried overnight at 50°C ,
133 after which they were counted at sea on a Risø[®] low-level beta GM multiscaler until
134 uncertainty was below 3%, and again 6 months later at home laboratory for background ^{234}Th
135 activities. After the second beta counting, filters were digested in an 8M HNO_3 /10% H_2O_2
136 solution (Carl Roth[®], trace metal grade). 10 dpm of ^{229}Th was added to each sample at the
137 beginning of digestion to achieve a 1:1 atom ratio between ^{229}Th : ^{230}Th . Digested samples
138 were diluted in a 2.5% HNO_3 /0.01% HF mixture and $^{229}\text{Th}/^{230}\text{Th}$ ratios were measured using

139 an ICP-MS (ThermoFisher® Element XR) to determine the chemistry yield and final ^{234}Th
140 activities. The average yield was calculated to be $97\% \pm 6\%$ ($n = 247$). For a subset of
141 samples (marked in Table S1) whose analysis failed during initial ICP-MS measurement,
142 anion chromatography (Biorad® AG1x8, 100 – 200 mesh, Poly-Prep columns) was performed
143 to remove Mn from the sample matrix before another ICP-MS analysis. This subset of
144 samples also included three samples (marked in Table S1) whose initial ICP-MS measurement
145 was successful, to test whether anion chromatography affects final ICP-MS results. Identical
146 $^{229}\text{Th}/^{230}\text{Th}$ ratios were measured for samples with and without column chromatography (see
147 Table S1 footnotes for details).

148 Each ^{238}U sample was acidified to pH ~ 1.6 at sea and transported home for analysis.
149 Samples of dissolved ^{238}U were diluted 20 times in 1N HNO_3 at home laboratory and spiked
150 with an appropriate amount of ^{236}U spike to achieve $^{236}\text{U}:^{238}\text{U} \sim 1:1$. Ratios of $^{236}\text{U}:^{238}\text{U}$ were
151 analyzed by ICP-MS (ThermoFisher Element XR) and activities of ^{238}U were calculated using
152 isotope dilution. Seawater certified reference materials (CRMs), CASS-6 and NASS-7, and
153 the International Association for the Physical Sciences of the Oceans (IAPSO) standard
154 seawater were analyzed routinely for uranium concentrations.

155

156 2.2 Flux calculation

157 Assuming a one box model, the temporal change of ^{234}Th activities is balanced by
158 production from ^{238}U , radioactive decay of ^{234}Th , removal of ^{234}Th onto sinking particles, and
159 transport into or out of the box by advection and diffusion (Bhat et al., 1968; Savoye et al.,
160 2006; and references therein):

$$161 \quad \frac{\partial A_{Th}}{\partial t} = \lambda(A_U - A_{Th}) - P + V \quad (1)$$

162 where A_U and A_{Th} are respectively the activities of dissolved ^{238}U and total ^{234}Th , λ is
 163 the decay constant of ^{234}Th , P is the net removal flux of ^{234}Th , and V is the sum of advective
 164 and diffusive fluxes. It is recommended that the time interval between station occupations
 165 should be >2 weeks in order to adequately capture the temporal variability of the mean spatial
 166 gradients rather than small local changes (Resplandy et al., 2012). The solution of Eq. (1)
 167 (Savoie et al., 2006) is

$$168 \quad P = \lambda \left[\frac{A_U(1-e^{-\lambda\Delta t}) + A_{Th1}e^{-\lambda\Delta t} - A_{Th2}}{1-e^{-\lambda\Delta t}} \right] \quad (2)$$

170 where Δt is the time interval between repeat occupations of a station; A_{Th1} and A_{Th2}
 171 are respectively total ^{234}Th activities during the first and second occupation. At times when
 172 repeat sampling is not possible within adequate cruise timeframe, steady state conditions are
 173 generally assumed, i.e. $\frac{\partial A_{Th}}{\partial t} = 0$. In this case, Eq. (1) is simplified into:

$$174 \quad P = \int_0^z \lambda(A_U - A_{Th})dz + V \quad (3)$$

175 The vertical flux of ^{234}Th , P ($\text{dpm m}^{-2} \text{d}^{-1}$), is integrated to the depth of interest. Earlier
 176 studies generally used arbitrarily fixed depths (e.g., the base of mixed layer or ML, and 100
 177 m) for ^{234}Th and POC flux estimates (e.g., Bacon et al., 1996; Buesseler et al., 1992). Recent
 178 studies emphasized the need to normalize POC flux to the depth of euphotic zone (EZ), which
 179 separates the particle production layer in the surface from the flux attenuation layer below
 180 (Black et al., 2018; Buesseler and Boyd, 2009; Rosengard et al., 2015). In the open ocean, the
 181 depth of EZ is generally similar to ML depth. The PAR (Photosynthetically Active Radiation)
 182 sensor was not available during both of our cruises, so that it was not possible to identify the
 183 base of the EZ. For the purpose of this study, the slight difference of the exact depth chosen
 184 (ML vs. EZ) was of little relevance to the significance of physical processes and ^{238}U
 185 variability.

186

187 2.3 Quantification of the physical fluxes

188 The physical term V in Eq. (2) is expressed as following:

$$189 \quad V = \int_0^z \left(w \frac{\partial Th}{\partial z} - u \frac{\partial Th}{\partial x} - v \frac{\partial Th}{\partial y} \right) dz + \int_0^z \left(K_x \frac{\partial^2 Th}{\partial x^2} + K_y \frac{\partial^2 Th}{\partial y^2} - K_z \frac{\partial^2 Th}{\partial z^2} \right) dz \quad (3)$$

190 where w is the vertical (i.e. upwelling) velocity (m s^{-1}), u and v respectively the zonal
191 and meridional current velocities (m s^{-1}), and K_x , K_y , and K_z represent eddy diffusivities ($\text{m}^2 \text{s}^{-1}$)
192 in zonal, meridional and vertical directions, respectively. $\frac{\partial Th}{\partial z}$, $\frac{\partial Th}{\partial x}$ and $\frac{\partial Th}{\partial y}$ are vertical and
193 horizontal ^{234}Th gradients ($\text{dpm L}^{-1} \text{m}^{-1}$), and $\frac{\partial^2 Th}{\partial x^2}$, $\frac{\partial^2 Th}{\partial y^2}$ and $\frac{\partial^2 Th}{\partial z^2}$ are respectively the second
194 derivative of ^{234}Th ($\text{dpm L}^{-1} \text{m}^{-2}$) on the zonal, meridional and vertical directions.

195

196 2.3.1 Estimation of upwelling velocities

197 In the Mauritanian and Peruvian coastal upwelling regions, there is strong evidence
198 that upwelling velocities in the mixed layer derived from satellite scatterometer winds and
199 Ekman divergence (Gill, 1982) agree well with those from helium isotope disequilibrium
200 (Steinfeldt et al., 2015). The parameterization by Gill (1982) considers the baroclinic response
201 of winds blowing parallel to a coastline in a two-layer ocean. Vertical velocity (w) at the
202 interface yields

$$203 \quad w = \frac{\tau}{\rho f a} e^{-x/a}$$

$$204 \quad (4)$$

205 where τ is the wind stress ($\text{kg m}^{-1} \text{s}^{-2}$) parallel to the coast line, ρ the water density (kg
206 m^{-3}), f the Coriolis parameter (s^{-1}), a the first baroclinic Rossby radius (km) and X the distance
207 (km) to the coast.

208 Upwelling velocities were calculated at stations within 60 nautical miles (nm) of the
209 coast, where upwelling is the most significant (Steinfeldt et al., 2015). We used $a = 15$ km for
210 all stations based on the results reported by Steinfeldt et al. (2015) for the same study area.
211 The magnitude of monthly wind stress was estimated from the monthly wind velocities
212 (Smith, 1988):

$$\tau = \rho_{air} C_D U^2$$

(5)

215 where ρ_{air} is the air density above the sea surface (1.225 kg m^{-3}), C_D the drag
216 coefficient (10^{-3} for wind speed $< 6 \text{ m s}^{-1}$), and U the wind speed.

217 Monthly wind speed (m s^{-1}) fields from MetOp-A/ASCAT scatterometer sensor with
218 a spatial resolution of 0.25° (Bentamy and Croize-Fillon, 2010) were retrieved from the
219 Centre de Recherche et d'Exploitation Satellitaire (CERSAT), at IFREMER, Plouzané
220 (France) (data version numbers L3-MWF-GLO-20170903175636-01.0 and L3-MWF-GLO-
221 20170903194638-01.0). We assumed a linear decrease of w from base of the mixed layer
222 toward both the ocean surface and 240 m depth (bottom depth of our shallowest station).
223 Upwelling rates at any depth between 0 and 240 m at individual station could thus be
224 determined once w was estimated. Following (Rapp et al., 2019), an error of 50% was
225 assigned to estimated upwelling velocities to account for uncertainties associated with the
226 spatial structure and temporal variability of the wind field, and the satellite wind product near
227 the coast.

228

229 2.3.2 Estimation of upper-ocean velocities

230 During both cruises a phased-array vessel-mounted acoustic Doppler current profiler
231 (VmADCP; 75 kHz Ocean Surveyor, Teledyne RD-Instruments) continuously measured zonal

232 and meridional velocities in the upper 700 m of the water column (Lüdke et al., in review
233 2020). Post-processing of the velocity data included water track calibration and bottom
234 editing. After calibration, remaining uncertainty of hourly averages of horizontal velocities are
235 smaller than 3 cm s^{-1} (e.g. Fischer et al., 2003). For the horizontal advective flux calculation
236 (Eq. 3), velocities collected within a 10 km radian at inshore stations (St. 353, 428, 458, 475,
237 508, 904, and 907) and within a 50 km radian at offshore stations were averaged. Data
238 collected at the same positions within 5 days due to station repeats were also included in the
239 velocity average. As representative for the near-surface flow, we extracted the velocity data
240 from the top 30 m for M136 stations and top 50 m for M138 station; these depths correspond
241 to 5-20 m below the base of the ML during each cruise.

242

243 2.3.3 Estimation of vertical and horizontal eddy diffusivities

244 While the strength of ocean turbulence determines the magnitude of diapycnal or
245 vertical eddy diffusivities, the intensity of meso- and submesoscale eddies determine the
246 magnitude of lateral eddy diffusivities. During the R/V Meteor cruise M136 and the follow up
247 cruise in the same region, the strength of upper-ocean turbulence was measured using shear
248 probes mounted to a microstructure profiler. The loosely-tethered profiler was optimized to
249 sink at a rate of 0.55 m s^{-1} and equipped with three shear sensors, a fast-response temperature
250 sensor, an acceleration sensor, two tilt sensors and conductivity, temperature, depth sensors
251 sampling with a lower response time. At most CTD stations 3 to 9 microstructure profiles
252 were collected. Standard processing procedures were used to determine the dissipation rate of
253 turbulent kinetic energy (ϵ) in the water column (see Schafstall et al., 2010 for detailed
254 description). Subsequently, turbulent vertical diffusivities K_z were determined from $K_z =$
255 $\Gamma \epsilon N^{-2}$ (Osborn, 1980), where N is stratification and Γ is the mixing efficiency for which a
256 value of 0.2 was used following Gregg et al. (2018). The 95% confidence intervals for

257 averaged K_z values were determined from Gaussian error propagation following Schafstall et
258 al. (2010).

259 Altogether, 189 microstructure profiles were collected during M136 (Thomsen and
260 Lüdke, 2018) and 258 profiles during the follow-up cruise M137 (unpublished data; May 6 –
261 29, 2017). An average turbulent vertical diffusivity profile was calculated from all inshore
262 (<500m water depth) and from all offshore (>500m water depth) profiles (Figure S1).
263 Microstructure profiles collected during cruise M138 were not available but there were little
264 variations amongst the cruise average inshore and offshore microstructure profiles from M136
265 and M137 despite drastic change in the intensities of the poleward Peru Chile Undercurrent
266 (Lüdke et al., in review 2020). It thus appears appropriate to apply these average vertical
267 diffusivities also to stations during M138.

268 Horizontal eddy diffusivity could not be determined from data collected during the
269 cruises. Surface eddy diffusivities in the North Atlantic OMZ were estimated to be on the
270 order of a few $1000 \text{ m}^2 \text{ s}^{-1}$ that decrease exponentially with depth (Hahn et al., 2014). Similar
271 magnitude of eddy diffusivities was estimated for the ETSP based on surface drifter data and
272 satellite altimetry (Abernathy and Marshall, 2013; Zhurbas and Oh, 2004). We thus consider
273 an eddy diffusivity of $1000 \text{ m}^2 \text{ s}^{-1}$ as a good approximate in this study for the evaluation of
274 horizontal diffusive ^{234}Th fluxes.

275

276 2.4 Residence time of ^{234}Th

277 The residence time ($\tau_{1/2}$) of total ^{234}Th represents a combination of the time required
278 for the partition of dissolved ^{234}Th onto particulate matter and that for particle removal. In a
279 one-box model, the residence time of an element of interest can be estimated by determining

280 the standing stock of this element and the rates of elemental input to the ocean or the rate of
281 element removal from seawater to sediments (Bewers and Yeats, 1977; Zimmerman, 1976):

$$\tau_{1/2} = \frac{A_{Th(mean)} \cdot Z}{P}$$

282
283 (6)

284 For the case of ^{234}Th , $A_{Th(mean)}$ is the averaged ^{234}Th activities of the surface layer, Z is
285 the depth of surface layer, and P the removal flux of ^{234}Th .

286

287 3. Results

288 3.1 Profiles of dissolved ^{238}U , total ^{234}Th , oxygen and fluorescence

289 The vertical profiles of ^{238}U and ^{234}Th activities are shown in Figure 2 and tabulated in
290 Table S1. Data from station 508 were reported in Figure 2 and Table S1 but excluded in the
291 Discussion section, because the surface sample at 5 m from this station was missing, which
292 prevents any flux calculation. Also tabulated in Table S1 are temperature, salinity and
293 concentrations of oxygen and fluorescence obtained from the CTD sensors. Uranium
294 concentrations of CRMs and the IAPSO standard seawater are reported in Table S2.

295 Activities of ^{238}U showed small to negligible variations with depth, averaging $2.54 \pm$
296 0.05 dpm L^{-1} (or $3.28 \pm 0.07 \text{ ng/g}$, 1SD, $n = 247$) at all stations. The vertical distributions of
297 ^{238}U did not appear to be affected by water column oxygen concentrations or the extent of
298 surface Chl a (Figure 2). Average U concentrations of both CASS-6 ($2.77 \pm 0.04 \text{ ng g}^{-1}$, 1SD,
299 $n = 5$) and NASS-7 ($2.86 \pm 0.05 \text{ ng/g}$, 1SD, $n = 5$) measured in this study agreed well with
300 certified values ($2.86 \pm 0.42 \text{ ng g}^{-1}$ and $2.81 \pm 0.16 \text{ ng g}^{-1}$, respectively). Average ^{238}U
301 concentration measured in our IAPSO standard seawater (OSIL batch P156) ($3.24 \pm 0.06 \text{ ng g}^{-1}$,
302 1 , 1SD, $n = 27$) is slightly higher than that reported in Owens et al. (2011) ($3.11 \pm 0.03 \text{ ng g}^{-1}$,

303 1SD, n = 10, OSIL P149), and may reflect slight differences in U concentrations between
304 different OSIL batches.

305 Total ^{234}Th varied from 0.63 to 2.89 dpm L⁻¹ (Figure 2). All stations showed large
306 ^{234}Th deficits in surface waters with $^{234}\text{Th}/^{238}\text{U}$ ratios as low as 0.25 (Figure 3). The extent of
307 surface ^{234}Th deficits did not vary as a function of depths of either mixed layer or the upper
308 oxic-anoxic interface, nor the magnitude of surface fluorescence concentrations (Table 1,
309 Figure 2). ^{234}Th at all stations generally reached equilibrium with ^{238}U at depths between 30 m
310 and 250 m. The equilibrium depths were slightly shallower toward the shelf at the 11°S, 12°S
311 and 16°S transects. At St. 912, deficits of ^{234}Th extended beyond 600 m depth (Figure 2). The
312 following stations (St. 428, 879, 898, 906, 907, 915, 919) displayed a secondary ^{234}Th deficit
313 below the equilibrium depth, indicative of ^{234}Th removal processes. A small ^{234}Th excess at
314 depth was only observed for St. 559 at 100 m. Ratios of $^{234}\text{Th}/^{238}\text{U}$ for deep samples at 1000
315 m, 1500 m, and 2000 m varied between 0.95 and 1.02 (1.00 ± 0.04 , 1SD, n = 11), suggesting
316 that ^{234}Th was at equilibrium with ^{238}U at these depths.

317

318 3.2 Vertical and horizontal ^{234}Th gradients

319 Discrete vertical ^{234}Th gradients in each profile (or the curvature of the profile) were
320 estimated by the difference in ^{234}Th activities and that in sampling depths. As such, vertical
321 ^{234}Th gradients varied greatly amongst stations, and were larger at shallow depths ranging
322 from 0.003 dpm L⁻¹ m⁻¹ to 0.085 dpm L⁻¹ m⁻¹ (median 0.013 dpm L⁻¹ m⁻¹). Vertical ^{234}Th
323 gradients were essentially negligible at and below equilibrium depths.

324 While calculation of the vertical ^{234}Th gradient is straightforward, the same is hardly
325 true for the determination of horizontal ^{234}Th gradient. Here we consider the top layer as top
326 30 m during M136 and top 50 m during M138. Mean ^{234}Th activities in the top layer of the

327 water column are highly variable amongst stations (Table 3, Figure 4), and likely reflect
328 variations occurring at small temporal and spatial scales in the Peruvian OMZ. Quantification
329 of the horizontal ^{234}Th gradient between individual station thus may not be adequate to
330 evaluate large scale advection and eddy diffusion across the study area. Therefore, alongshore
331 ^{234}Th gradients on a larger spatial scale (1° apart) were instead calculated by grouping stations
332 into 1° by 1° grids and averaging ^{234}Th activities of each grid for the top layer. Alongshore
333 ^{234}Th gradients in the top layer at nearshore stations for M138 are fairly consistent, ranging
334 from $1.5 \times 10^{-6} \text{ dpm L}^{-1} \text{ m}^{-1}$ to $1.7 \times 10^{-6} \text{ dpm L}^{-1} \text{ m}^{-1}$, with a slightly stronger gradient in the
335 north compared to the south. The net difference in alongshore ^{234}Th gradient is merely 2×10^{-7}
336 $\text{dpm L}^{-1} \text{ m}^{-1}$. A slightly smaller alongshore ^{234}Th gradient of $4.8 \times 10^{-7} \text{ dpm L}^{-1} \text{ m}^{-1}$ was
337 observed for M136. The magnitude of the net difference in alongshore ^{234}Th gradient for
338 M136 cannot be adequately quantified, due to smaller spatial sampling coverage. Judging on
339 the similarity in the spatial distributions of mean ^{234}Th between cruises M136 and M138, it is
340 reasonable to assume that net difference in alongshore ^{234}Th gradient remained similar during
341 both cruises.

342

343 3.3 Steady state vs. non-steady state models

344 The relative importance of ^{234}Th fluxes due to advection and diffusion were assessed
345 here assuming steady state conditions, which assume negligible temporal ^{234}Th variability.
346 But how valid is this assumption in the Peruvian upwelling zone? Profiles of temperature and
347 oxygen at repeat stations 458 and 508 showed that a lightly cooler and oxygen-depleted water
348 mass dominated at the upper 50 m at station 508 (Figure 5). However, an assessment of the
349 ^{234}Th fluxes at these two stations were not possible as the surface sample from station 508 was
350 missing. Repeat stations 495 and 516 show substantial temporal variations in ^{234}Th activities
351 at each sampled depth in the top 200 m, while temperature and salinity profiles confirmed that

352 similar water masses were sampled during both occupations (Figure 5). Particularly, the
353 surface ^{234}Th deficit was more intense at St. 495 ($^{234}\text{Th}/^{238}\text{U} = 0.44$) compared to St. 516
354 ($^{234}\text{Th}/^{238}\text{U} = 0.73$). Correspondingly, ^{234}Th fluxes decreased substantially from St. 495 to St.
355 516. At 100 m, the difference in ^{234}Th fluxes between these two stations was $\sim 30\%$ ($3200 \pm$
356 $90 \text{ dpm m}^{-2} \text{ d}^{-1}$ at St. 495 and $2230 \pm 110 \text{ dpm m}^{-2} \text{ d}^{-1}$ at St. 516). At 200 m where ^{234}Th
357 resumed equilibrium with ^{238}U at both stations, ^{234}Th flux difference was $\sim 25\%$ (4510 ± 220
358 $\text{dpm m}^{-2} \text{ d}^{-1}$ at St. 495 and $3455 \pm 200 \text{ dpm m}^{-2} \text{ d}^{-1}$ at St. 516). Taking the non-steady state
359 term in Eq. (1) into consideration (see details in Resplandy et al. (2012) and Savoye et al.
360 (2006) for the derivation of flux formulation and error propagation) increased total ^{234}Th at St.
361 516 by 40% to $3110 \pm 1870 \text{ dpm m}^{-2} \text{ d}^{-1}$ at 100 m (or 45% to $5040 \pm 2290 \text{ dpm m}^{-2} \text{ d}^{-1}$ at 200
362 m), which is indistinguishable within error from fluxes at St. 495. The large errors associated
363 with the non-steady state calculation prevent a meaningful application of this model in the
364 current study (also see discussion in Resplandy et al, 2012). As estimation of the physical
365 fluxes is independent of the models chosen between steady and non-steady states, the
366 following results and discussion sections regarding physical effects on the ^{234}Th flux estimates
367 is based on the steady state model only.

368

369 3.4 Export fluxes of ^{234}Th

370 Fluxes of ^{234}Th due to radioactive production and decay (hereafter ‘production flux’),
371 upwelling, and vertical diffusion were reported in Table 1 and Figure 6 for both depths 5-20
372 m below the ML and at 100 m. Due to sampling logistics, we did not sample at the base of the
373 ML, but 5-20 m below the ML. This depth corresponded closely to the EZ depth used in
374 Black et al. (2018) in the same study area during austral summer 2013. For the purpose of
375 comparison with earlier studies which reported ^{234}Th fluxes at 100 m, we also calculated ^{234}Th
376 fluxes at 100 m in this study. The production fluxes of ^{234}Th at 5-20 m below the ML ranged

377 from $560 \text{ dpm m}^{-2} \text{ d}^{-1}$ to $1880 \text{ dpm m}^{-2} \text{ d}^{-1}$, whereas at 100 m they were much higher at 850
378 $\text{dpm m}^{-2} \text{ d}^{-1}$ to $3370 \text{ dpm m}^{-2} \text{ d}^{-1}$. There is no discernable trend regarding the production fluxes
379 between the shelf and offshore stations, similar to those seen along the eastern GP16 transect
380 (Black et al. 2017).

381 Alongshore winds were unusually weak off Peru preceding and during our sampling
382 campaign as a result of the 2017 coastal El Niño (Echevin et al., 2018; Lüdke et al., in review
383 2020; Peng et al., 2019), which resulted in nominal upwelling in the water column. At
384 nearshore stations, upwelling rates at the base of the ML varied between $1.3 \times 10^{-7} \text{ m s}^{-1}$ and
385 $9.7 \times 10^{-6} \text{ m s}^{-1}$, whereas upwelling rates at offshore stations were on the order of $10^{-10} \text{ m s}^{-1}$
386 to 10^{-8} m s^{-1} and essentially negligible. As a result, upwelled ^{234}Th fluxes at 5-20 m below the
387 ML were only significant at stations closest to shore; these stations were 428 ($130 \text{ dpm m}^{-2} \text{ d}^{-1}$)
388 1), 883-12 ($80 \text{ dpm m}^{-2} \text{ d}^{-1}$) and 904-16 ($280 \text{ dpm m}^{-2} \text{ d}^{-1}$) whose upwelled ^{234}Th fluxes
389 accounted for 10%, 11% and 25% of the total ^{234}Th fluxes respectively (Figure 6). Upwelled
390 ^{234}Th fluxes at the rest of the stations accounted for less than 2% of the total ^{234}Th fluxes (6%
391 at stations 353 and 907-11) and were insignificant. At 100 m, both vertical ^{234}Th gradients and
392 upwelling rates were significantly smaller compared to shallower depths. As a result,
393 upwelled ^{234}Th fluxes were less than $70 \text{ dpm m}^{-2} \text{ d}^{-1}$, or less than 4% of total ^{234}Th fluxes.

394 Similarly, vertical diffusivities, shown as running mean over 20 m in Figure S1, were
395 an order of magnitude higher at shallow stations ($3.2 \times 10^{-4} \pm 1.7 \times 10^{-4} \text{ m}^2 \text{ s}^{-1}$; 1SD, 27 m to
396 100 m below sea surface) compared to those at deep stations ($1.7 \times 10^{-5} \pm 0.6 \times 10^{-5} \text{ m}^2 \text{ s}^{-1}$;
397 1SD; 34 – 100 m below sea surface). Within the 27 m to 33 m layer at deep stations, vertical
398 diffusivities decreased exponentially by an order of magnitude within a few meters; below
399 this depth, vertical diffusivities remained relatively stable (Figure S1). This is not surprising
400 as wind-driven turbulent is most significant at the ocean surface (Buckingham et al., 2019). In
401 this study, the sampling depths immediately below the ML were generally 30 m and 60 m. A

402 few high vertical diffusivity values around 30 m at deep stations were unlikely representative
403 for the 30 m – 60 m water column layer. We thus opted to only apply vertical diffusivities
404 below 33 m at deep stations. Relative standard errors (RSE) associated with diffusivity
405 estimates varied from 35% to 55%. Vertical diffusive ^{234}Th fluxes at 5-20 m below the ML,
406 determined using both vertical diffusivity and vertical ^{234}Th gradient, varied greatly amongst
407 stations. At shallow stations 428, 458, and 883-12, vertical diffusive ^{234}Th fluxes made up
408 37% ($490 \text{ dpm m}^{-2} \text{ d}^{-1}$), 14% ($160 \text{ dpm m}^{-2} \text{ d}^{-1}$), and 21% ($160 \text{ dpm m}^{-2} \text{ d}^{-1}$) of total ^{234}Th
409 fluxes, respectively (Figure 6). At the rest of the stations, vertical diffusive ^{234}Th fluxes
410 appeared to be insignificant, ranging between 1% and 10% in the total ^{234}Th flux budget. At
411 100 m, vertical diffusive ^{234}Th fluxes at station 428, 458, and 883-12 remained high at 390
412 $\text{dpm m}^{-2} \text{ d}^{-1}$, $150 \text{ dpm m}^{-2} \text{ d}^{-1}$, $120 \text{ dpm m}^{-2} \text{ d}^{-1}$, respectively, whereas those at the rest of the
413 stations accounted for < 2% of the total ^{234}Th flux.

414 Horizontal advective and diffusive ^{234}Th fluxes were both very small. Average
415 alongshore current velocities (Lüdke et al., in review 2020) for the surface layer varied from
416 0.06 m s^{-1} to 0.34 m s^{-1} . At the peripheral of a freshly-formed anticyclonic eddy (St. 915-1),
417 alongshore current velocities could be as high as 0.53 m s^{-1} . Taking the mean alongshore
418 velocity of 0.2 m s^{-1} and the net difference in alongshore ^{234}Th gradient of $2 \times 10^{-7} \text{ dpm L}^{-1} \text{ m}^{-1}$,
419 the resulting net horizontal advective ^{234}Th flux is $\sim 50 \text{ dpm m}^{-2} \text{ d}^{-1}$, a mere 3-9% of the
420 total ^{234}Th fluxes.

421 Horizontal diffusive ^{234}Th flux was estimated using an average eddy diffusivity of
422 $1000 \text{ m}^2 \text{ s}^{-1}$ (see Methods section 2.3.3) and the alongshore ^{234}Th gradient. A maximum value
423 of $10 \text{ dpm m}^{-2} \text{ d}^{-1}$ was calculated, which accounted for <1% of total ^{234}Th flux at all stations.
424 Note that the horizontal advective and lateral diffusive fluxes presented here are a rough
425 estimate and should only provide an idea of their order of magnitude. Due to the uncertainty
426 inherent to the estimates, we refrain from adding these values to Table 1.

427

428 **4. Discussion**

429 4.1 Lack of linear ^{238}U – salinity correlation in the Peruvian OMZ

430 The water column profiles of ^{238}U in the Peruvian OMZ (Figure 2) are similar to those
431 seen in the open ocean (see compilations in Owens et al., 2011 and Van Der Loeff et al.
432 (2006), and references therein). It thus appears that water column suboxic/anoxic conditions
433 alone is not sufficient to remove U, in contrast to sedimentary U studies underlying low
434 oxygen waters where soluble U(VI) diffused downward into subsurface sediments and
435 reduced to insoluble U(IV) (Anderson et al., 1989; Böning et al., 2004; Scholz et al., 2011).
436 Our inference is in accord with water column ^{238}U studies in intense OMZs in the eastern
437 tropical North Pacific (Nameroff et al., 2002) and the Arabian Sea (Rengarajan et al., 2003),
438 where ^{238}U concentrations remain constant over the entire upper water column studied.

439 Dissolved ^{238}U and salinity across the entire Peruvian OMZ displayed poor linear
440 correlation regardless of seawater oxygen concentrations (Figure 7a-b). The general consensus
441 is that U behaves conservatively in oxic seawater in the open ocean and early observations
442 have shown that ^{238}U activities can be calculated from salinity based on a simple linear
443 correlation between the two (e.g. Chen et al., 1986; Ku et al., 1977). Recent compilations in
444 Van Der Loeff et al. (2006) and Owens et al. (2011) further demonstrated that the majority of
445 uranium data points in the global seawater dataset follow a linear correlation with seawater
446 salinity. The ^{238}U -salinity formulations from either Chen et al. (1986) or Owens et al. (2011)
447 are thus generally appropriate for open ocean conditions and have been widely used in ^{234}Th
448 flux studies. However, this linear ^{238}U -salinity correlation breaks down in the Peruvian OMZ.
449 Furthermore, the measured ^{238}U activities in this study correlated poorly with those calculated
450 from salinity using the Owens formulation regardless of water column oxygen concentrations
451 (Table S2, Figure 7c), with the former significantly higher than the projected values and

452 differences up to 10%. Both evidences suggested that non-conservative processes have
453 introduced significant amount of dissolved U into the water column.

454 It is likely that this poor ^{238}U -salinity correlation in the water column is not a unique
455 feature off the coast of Peru. Poor correlations between dissolved ^{238}U and salinity have been
456 previously observed in open ocean settings such as the Arabian Sea (Rengarajan et al., 2003)
457 and the Pacific Ocean (Ku et al., 1977), and shelf-estuary systems such as the Amazon shelf
458 (McKee et al., 1987; Swarzenski et al., 2004). It is possible that the narrow range of salinity
459 within any single ocean basin precludes a meaningful ^{238}U -salinity correlation (Ku et al.,
460 1977; Owens et al., 2011). For the Peruvian shelf system, two possible scenarios may further
461 explain the lack of linear ^{238}U -salinity correlation in the water column. Firstly, authigenic U
462 within the sediments may be remobilized under ENSO-related oxygenation events. Pore water
463 and bottom water geochemistry measurements during two previous cruises (M77-1 and M77-
464 2) along an 11°S transect off Peru showed large diffusive fluxes of U out of the Peruvian shelf
465 sediments despite that both Fe reduction and U reduction took place in the top centimeters of
466 sediments (Scholz et al., 2011). It was suggested that a minute increase in bottom water
467 oxygen concentration induced by El Niño events would be sufficient in shifting the
468 U(VI)/U(IV) boundary by a few centimeters and remobilize authigenic U (Scholz et al.,
469 2011). Preceding and during our sampling campaign, a coastal El Niño event, with coastal
470 precipitation as strong as the 1997-98 El Niño event, had developed rapidly and unexpectedly
471 in January, and disappeared by May 2017 during cruise M136 (Echevin et al., 2018;
472 Garreaud, 2018; Peng et al., 2019). This strong coastal El Niño event could induce an
473 oxygenation event large enough to remobilized authigenic U along the Peruvian shelf.
474 Secondly, resuspension of bottom sediments and subsequent desorption of U from ferric-
475 oxyhydroxides could affect the ^{238}U -salinity relationship, similar to that seen on the Amazon
476 shelf at salinity above 10 (McKee et al., 1987) and in laboratory experiments (Barnes and

477 Cochran, 1993). Fe reduction and release from the Peruvian shelf sediments (Noffke et al.,
478 2012; Scholz et al., 2014) could release additional U to overlying waters. The magnitude of
479 such, however, has not been quantified.

480 The consequence of the notable difference between measured ^{238}U in this study and
481 salinity-based ^{238}U to ^{234}Th flux according to Eq. (2) is neither linear nor straightforward,
482 because the vertical gradients of both ^{238}U and ^{234}Th strongly affects the impacts of ^{238}U
483 variations on ^{234}Th fluxes. In this study, ^{234}Th fluxes at 100 m derived from salinity-based
484 ^{238}U lead to significant underestimation of ^{234}Th fluxes by an average of 20% and as high as
485 40% (Table 2). These differences in ^{234}Th fluxes will have direct consequences for ^{234}Th
486 derived elemental fluxes such as C, N, P and trace metals. It is thus important to note that U
487 concentrations in coastal systems are highly sensitive to bottom water oxygen concentrations
488 and redox-related U addition, variability of which is expected to intensify with future climate
489 change (Shepherd et al., 2017). Relatively minor variations in dissolved ^{238}U could account
490 for substantial overestimation/underestimation of the depth-integrated ^{234}Th fluxes. We thus
491 encourage future ^{234}Th flux studies in such environments to include seawater ^{238}U analysis.

492

493 4.2 Dynamic advective and diffusive ^{234}Th fluxes

494 The significance of advection and diffusion in the total ^{234}Th flux budget highly
495 depends on the upwelling rate, current velocity, vertical diffusivity, and ^{234}Th gradient on the
496 horizontal and vertical directions. Our results demonstrated that physical processes off Peru
497 during and post the 2017 coastal El Nino have very limited impact on the downward fluxes of
498 ^{234}Th (Figure 6).

499 Our findings are in reasonable agreement with those from the GEOTRACES GP16
500 eastern section along 12°S from Peru to Tahiti, in which Black et al. (2018) quantified both

501 horizontal and vertical advective ^{234}Th fluxes. Horizontal advective fluxes for the upper 30 m
502 water column estimated during GP16 were $\sim 180 \text{ dpm m}^{-2} \text{ d}^{-1}$ for all nearshore and offshore
503 stations, similar in magnitude to those estimated in our study. Upwelling fluxes along GP16
504 eastern section was suggested to account for 50% to 80% of total ^{234}Th fluxes at the base of
505 the euphotic zone (at similar depths or slightly deeper than ML depths in the current study)
506 (Black et al., 2018). Total ^{234}Th fluxes along the GP16 eastern section, ranging from 4000 to
507 5000 $\text{dpm m}^{-2} \text{ d}^{-1}$ at the base of the euphotic zone, were much higher than those in our study
508 (560 to 1900 $\text{dpm m}^{-2} \text{ d}^{-1}$ at the base of the ML). This difference could be related to the period
509 of sampling (austral autumn and winter 2017 in our study *vs.* austral summer 2013 for the
510 GP16 section). We note that the estimated vertical mixing rates based on ^7Be isotope at the
511 base of the euphotic zone along the GP16 section (Kadko, 2017) were at least an order of
512 magnitude higher than the upwelling rates at the base of the ML at nearby stations in our
513 study. This difference could stem from different methods used to estimate upwelling rates at
514 different timescales, and may also reflect the dynamic upwelling system off Peru in which
515 upwelling rates vary greatly seasonally and interannually. During cruises M136 and M138,
516 upwelling favorable easterly winds off Peru were weak, resulting in negligible coastal
517 upwelling. Coastal upwelling in the same general area was also suggested to be negligible in
518 austral summer 2013 during cruise M92 due to nominal surface wind stress (Thomsen et al.,
519 2016). Results from studies conducted in the same year (October to December 2013, Kadko,
520 2017; December 2012, Steinfeldt et al., 2015) indicate that seasonal upwelling rates vary
521 drastically in the Peruvian upwelling zone. The seasonal dynamics of coastal upwelling off
522 Peru are similar to those seen in the Arabian Sea, where large upwelled ^{234}Th fluxes only
523 occurred during mid-late southwest monsoon at stations close to shore (Buesseler et al.,
524 1998). Our findings lend further support to earlier studies that advection and diffusion are
525 seasonally important for ^{234}Th fluxes in regions with high upwelling velocities and
526 diffusivities such as the equatorial Pacific (Bacon et al., 1996; Buesseler et al., 1995; Dunne

527 and Murray, 1999) and coastal sites such as the Arabian Sea (Buesseler et al., 1998) and
528 offshore Peru (Black et al., 2018; this study).

529

530 4.3 Residence time of ^{234}Th in the Peruvian OMZ

531 The residence time calculated using equation (6) was based on a simplified one-
532 dimension (1D) model of Zimmerman (1976). This 1D steady state model is obviously an
533 oversimplification of a multi-dimensional process, it however provides a good first order
534 estimate for understanding the highly dynamic nature of the ^{234}Th residence time. It also
535 provides a reasonable value that can be directly compared to values estimated in earlier ^{234}Th
536 flux studies that did not consider the physical processes. Furthermore, we showed in the
537 Discussion (sections 4.2) that physical processes, namely upwelling and vertical diffusion, are
538 only important at a few shelf stations. We thus consider this simple 1D model robust in
539 estimating the residence time of total ^{234}Th .

540 In this study, residence time of total ^{234}Th in the surface layer (top 30 m during M136
541 and top 50 m during M138) varied from 20 days at shallow stations to 95 days at deep stations
542 (mean $\tau = 51 \pm 23$ days, 1SD, $n = 24$; Table 3). These values were similar to those estimated
543 within the California Current (Coale and Bruland, 1985) and the residence times of particulate
544 organic carbon (POC) and nitrogen (PON) (Murray et al., 1989), but were much longer than
545 predicted in nearshore shelf waters where residence times of total ^{234}Th were on the order of a
546 few days (Kaufman et al., 1981; Kim et al., 1999; and references therein). The longer
547 residence times estimated in our study could reflect a combination of weak surface ^{234}Th
548 deficits ($^{234}\text{Th} = 0.63$ to 1.82 dpm L^{-1}) (Figure 3) and low export fluxes (800 to 2000 dpm m^{-2}
549 d^{-1} , Figure 7). Nearshore seawater samples during GP16 (Black et al., 2018) featured similar
550 surface ^{234}Th deficits ($^{234}\text{Th} = 0.63$ to 1.33 dpm L^{-1}) but much higher downward ^{234}Th fluxes
551 (4000 to 5000 dpm $\text{m}^{-2} \text{d}^{-1}$) as a result of strong upwelling, implying that residence times of

552 total ^{234}Th in the Peruvian OMZ during GP16 occupation would be 3 – 6 times shorter.
553 Indeed, a quick re-assessment of the GP16 data predicted a shorter residence time of total
554 ^{234}Th of 5 – 23 days within the euphotic zone of the coastal Peruvian OMZ.

555 These temporal variations on the residence times of total ^{234}Th have important
556 implications for the estimation of POC fluxes and quantification of carbon export efficiency.
557 Firstly, seasonal changes in Th residence times reflect variations in particle removal over
558 different integrated timescales. For example, POC produced in surface waters during GP16
559 (austral summer 2013) (Black et al., 2018) would have been exported out of the euphotic zone
560 3-6 times faster than it did during austral autumn 2017 (this study). Secondly, to properly
561 evaluate carbon export efficiency, surface net primary production (NPP) should be averaged
562 over a similar timescale as the residence time of total ^{234}Th during station occupation.
563 Applying a 16-day averaged NPP for export efficiency estimate (Black et al., 2018; Henson et
564 al., 2011) would likely not be appropriate in the current study in which total ^{234}Th fluxes
565 integrated timescales of several weeks. ^{234}Th residence times should thus be properly
566 quantified in coastal studies before deriving export efficiencies over varying NPP integration
567 timescales.

568

569 **5. Conclusions and implications for coastal ^{234}Th flux studies**

570 Advection and diffusion are important in coastal and upwelling regions with respect to
571 ^{234}Th export fluxes (Bacon et al., 1996; Buesseler et al., 1995; Dunne and Murray, 1999;
572 Buesseler et al., 1998). Our findings show that their significance is subject to the seasonal
573 variability of the current and upwelling velocities, diffusivities and ^{234}Th gradients, and
574 should be evaluated on a case-to-case basis. Advective fluxes are perhaps the most
575 straightforward to estimate as current velocities can be obtained routinely from shipboard
576 ADCP measurements and upwelling rates calculated from satellite wind stress (Steinfeldt et

577 al., 2015; Bacon et al., 1996). Horizontal and vertical velocities derived from general ocean
578 circulation models also provide a good first order estimate for advective ^{234}Th fluxes; this
579 approach has been successfully demonstrated in a few studies (Buesseler et al., 1995;
580 Buesseler et al., 1998). In addition, the anthropogenic SF_6 tracer and radium isotopes, widely
581 used to quantify nutrient and Fe fluxes (Charette et al., 2007; Law et al., 2001), as well as ^7Be
582 isotope (Kadko, 2017), could be used independently to constrain horizontal and vertical
583 exchange rates of ^{234}Th (Morris et al., 2007; Charette et al., 2007; Buesseler et al., 2005).
584 When *in situ* microstructure measurements are available (this study), vertical diffusivity can
585 be directly calculated to estimate the vertical diffusive ^{234}Th fluxes. Yet, microstructure
586 analysis is not a routine measurement on oceanographic cruises. Earlier studies in the
587 equatorial Pacific and the Gulf of Maine have shown that general ocean circulation models
588 and a simple assumption on dissipation coefficients could provide a robust estimate on
589 vertical and horizontal diffusivities (Benitez-Nelson et al., 2000; Gustafsson et al., 1998;
590 Charette et al., 2001). Therefore, the calculation of physical fluxes is possible, though
591 challenging, and ^{234}Th fluxes due to physical processes should be carefully considered when
592 conducting research in a coastal and upwelling systems.

593 A striking finding in this study is that the assumption of a linear ^{238}U -salinity
594 correlation could lead to one of the largest errors in ^{234}Th flux estimates. In our study, using
595 the salinity-based ^{238}U activities resulted in significant underestimation of total ^{234}Th fluxes by
596 as much as 40%. Because the translation of ^{238}U activities to ^{234}Th fluxes is not linear, larger
597 differences between measured and salinity-based ^{238}U do not necessarily contribute to greater
598 overestimation or underestimation of ^{234}Th fluxes. For example, moderate difference of 3-6%
599 in ^{238}U throughout the upper 100 m at station 898 lead to 40% difference in final ^{234}Th flux,
600 while a 5-9% difference in ^{238}U at station 906 only resulted in 16% ^{234}Th flux difference

601 (Table 2, S2). We would thus stress the importance of ^{238}U measurements in future ^{234}Th flux
602 studies particularly in coastal and shelf regions.

603 Finally, our study showed that the residence times of total ^{234}Th in the Peruvian
604 nearshore waters varied seasonally. Tropical OMZs are important hotspots for carbon
605 sequestration from the atmosphere and enhanced sedimentary carbon preservation (Arthur et
606 al., 1998; Suess et al., 1987). These OMZs are projected to intensify as a result of future
607 climate change (Keeling and Garcia, 2002; Schmidtko et al., 2017; Stramma et al., 2008).
608 Future studies should take into consideration the large temporal variations of the residence
609 times of total ^{234}Th in order to properly evaluates how carbon biogeochemical cycles and
610 carbon export efficiency in these OMZs will respond to continuing ocean deoxygenation,

611

612 **Data availability**

613 Data are available in supplementary tables and will be archived in Pangea upon
614 publication of the article.

615

616 **Author contribution**

617 RCX, FACLM and EAP designed the study. RCX carried out sampling, on-board beta
618 counting of ^{234}Th , and drafted the manuscript. IR conducted ^{234}Th and ^{238}U analyses at home
619 laboratory. JL computed current velocities and vertical diffusivities respectively from
620 VmADCP and microstructure profiler data. All co-authors had a chance to review the
621 manuscript and contributed to discussion and interpretation of the data presented.

622

623 **Competing interests**

624 The authors declare that they have no conflict of interest.

625

626 **Acknowledgements**

627 We thank the crew and science party on board M136 and M138 for their help in sample
628 collection and instrument operation. Thank you to SiaoJean Ko, Dominik Jasinski, André
629 Mutzberg and Mario Esposito for their laboratory assistance. We thank two anonymous
630 reviewers and the associate editor, Marilaure Grégoire, for their constructive comments. The
631 project, cruises, IR, JL and RCX were funded by the German SFB 754 program ('Climate-
632 Biogeochemistry Interactions in the Tropical Ocean'), and FACLM by a DFG Fellowship of
633 the Excellence Cluster "The Future Ocean" (CP1403). This manuscript benefited from
634 stimulating discussions at the BIARRITZ ('bridging international activity and related research
635 into the twilight zone') workshop held in Southampton, UK in 2019.

References

- 636
637
638 Abernathey, R. P., and Marshall, J.: Global surface eddy diffusivities derived from satellite
639 altimetry, *Journal of Geophysical Research: Oceans*, 118, 901-916,
640 <https://doi.org/10.1002/jgrc.20066>, 2013.
- 641 Anderson, R. F., Fleisher, M. Q., and LeHuray, A. P.: Concentration, oxidation state, and
642 particulate flux of uranium in the Black Sea, *Geochimica et Cosmochimica Acta*, 53, 2215-
643 2224, [https://doi.org/10.1016/0016-7037\(89\)90345-1](https://doi.org/10.1016/0016-7037(89)90345-1), 1989.
- 644 Arthur, M. A., Dean, W. E., and Laarkamp, K.: Organic carbon accumulation and
645 preservation in surface sediments on the Peru margin, *Chemical Geology*, 152, 273-286,
646 [https://doi.org/10.1016/S0009-2541\(98\)00120-X](https://doi.org/10.1016/S0009-2541(98)00120-X), 1998.
- 647 Bacon, M., Cochran, J., Hirschberg, D., Hammar, T., and Fler, A.: Export flux of carbon at
648 the equator during the EqPac time-series cruises estimated from ^{234}Th measurements, *Deep*
649 *Sea Research Part II: Topical Studies in Oceanography*, 43, 1133-1153,
650 [https://doi.org/10.1016/0967-0645\(96\)00016-1](https://doi.org/10.1016/0967-0645(96)00016-1), 1996.
- 651 Barnes, C. E., and Cochran, J. K.: Uranium geochemistry in estuarine sediments: Controls on
652 removal and release processes, *Geochimica et Cosmochimica Acta*, 57, 555-569,
653 [https://doi.org/10.1016/0016-7037\(93\)90367-6](https://doi.org/10.1016/0016-7037(93)90367-6), 1993.
- 654 Benitez-Nelson, C. R., Buesseler, K. O., and Crossin, G.: Upper ocean carbon export,
655 horizontal transport, and vertical eddy diffusivity in the southwestern Gulf of Maine,
656 *Continental Shelf Research*, 20, 707-736, [https://doi.org/10.1016/S0278-4343\(99\)00093-X](https://doi.org/10.1016/S0278-4343(99)00093-X),
657 2000.
- 658 Bentamy, A., and Croize-Fillon: Gridded surface wind fields from Metop/ASCAT
659 measurements, *International Journal of Remote Sensing*, doi:10.1080/01431161.2011.600348,
660 2010.
- 661 Bewers, J., and Yeats, P.: Oceanic residence times of trace metals, *Nature*, 268, 595-598,
662 1977.

663 Bhat, S., Krishnaswamy, S., Lal, D., and Moore, W.: $^{234}\text{Th}/^{238}\text{U}$ ratios in the ocean, Earth and
664 Planetary Science Letters, 5, 483-491, [https://doi.org/10.1016/S0012-821X\(68\)80083-4](https://doi.org/10.1016/S0012-821X(68)80083-4), 1968.

665 Black, E. E., Buesseler, K. O., Pike, S. M., and Lam, P. J.: ^{234}Th as a tracer of particulate
666 export and remineralization in the southeastern tropical Pacific, Marine Chemistry, 201, 35-
667 50, <https://doi.org/10.1016/j.marchem.2017.06.009>, 2018.

668 Black, E. E., Lam, P. J., Lee, J. M., and Buesseler, K. O.: Insights From the ^{238}U - ^{234}Th
669 Method Into the Coupling of Biological Export and the Cycling of Cadmium, Cobalt, and
670 Manganese in the Southeast Pacific Ocean, Global Biogeochemical Cycles, 33, 15-36,
671 <https://doi.org/10.1029/2018GB005985>, 2019.

672 Böning, P., Brumsack, H.-J., Böttcher, M. E., Schnetger, B., Kriete, C., Kallmeyer, J., and
673 Borchers, S. L.: Geochemistry of Peruvian near-surface sediments, Geochimica et
674 Cosmochimica Acta, 68, 4429-4451, <https://doi.org/10.1016/j.gca.2004.04.027>, 2004.

675 Buckingham, C. E., Lucas, N. S., Belcher, S. E., Rippeth, T. P., Grant, A. L. M., Le Sommer,
676 J., Ajayi, A. O., and Naveira Garabato, A. C.: The Contribution of Surface and Submesoscale
677 Processes to Turbulence in the Open Ocean Surface Boundary Layer, Journal of Advances in
678 Modeling Earth Systems, 11, 4066-4094, <https://doi.org/10.1029/2019MS001801>, 2019.

679 Buesseler, K., Ball, L., Andrews, J., Benitez-Nelson, C., Belostock, R., Chai, F., and Chao,
680 Y.: Upper ocean export of particulate organic carbon in the Arabian Sea derived from
681 thorium-234, Deep Sea Research Part II: Topical Studies in Oceanography, 45, 2461-2487,
682 [https://doi.org/10.1016/S0967-0645\(98\)80022-2](https://doi.org/10.1016/S0967-0645(98)80022-2), 1998.

683 Buesseler, K. O., Bacon, M. P., Cochran, J. K., and Livingston, H. D.: Carbon and nitrogen
684 export during the JGOFS North Atlantic Bloom Experiment estimated from ^{234}Th : ^{238}U
685 disequilibria, Deep Sea Research Part A. Oceanographic Research Papers, 39, 1115-1137,
686 [https://doi.org/10.1016/0198-0149\(92\)90060-7](https://doi.org/10.1016/0198-0149(92)90060-7), 1992.

687 Buesseler, K. O., Andrews, J. A., Hartman, M. C., Belostock, R., and Chai, F.: Regional
688 estimates of the export flux of particulate organic carbon derived from thorium-234 during the

689 JGOFS EqPac program, Deep Sea Research Part II: Topical Studies in Oceanography, 42,
690 777-804, [https://doi.org/10.1016/0967-0645\(95\)00043-P](https://doi.org/10.1016/0967-0645(95)00043-P), 1995.

691 Buesseler, K. O., Andrews, J., Pike, S. M., Charette, M. A., Goldson, L. E., Brzezinski, M. A.,
692 and Lance, V.: Particle export during the southern ocean iron experiment (SOFeX),
693 Limnology and Oceanography, 50, 311-327, <https://doi.org/10.4319/lo.2005.50.1.0311>, 2005.

694 Buesseler, K. O., Benitez-Nelson, C. R., Moran, S., Burd, A., Charette, M., Cochran, J. K.,
695 Coppola, L., Fisher, N., Fowler, S., and Gardner, W.: An assessment of particulate organic
696 carbon to thorium-234 ratios in the ocean and their impact on the application of ^{234}Th as a
697 POC flux proxy, Marine Chemistry, 100, 213-233,
698 <https://doi.org/10.1016/j.marchem.2005.10.013>, 2006.

699 Buesseler, K. O., and Boyd, P. W.: Shedding light on processes that control particle export
700 and flux attenuation in the twilight zone of the open ocean, Limnology and Oceanography, 54,
701 1210-1232, <https://doi.org/10.4319/lo.2009.54.4.1210>, 2009.

702 Cai, P., Chen, W., Dai, M., Wan, Z., Wang, D., Li, Q., Tang, T., and Lv, D.: A high -
703 resolution study of particle export in the southern South China Sea based on ^{234}Th : ^{238}U
704 disequilibrium, Journal of Geophysical Research: Oceans, 113, 2008.

705 Charette, M. A., Moran, S. B., Pike, S. M., and Smith, J. N.: Investigating the carbon cycle in
706 the Gulf of Maine using the natural tracer thorium 234, Journal of Geophysical Research:
707 Oceans, 106, 11553-11579, <https://doi.org/10.1029/1999JC000277>, 2001.

708 Charette, M. A., Gonnee, M. E., Morris, P. J., Statham, P., Fones, G., Planquette, H., Salter,
709 I., and Garabato, A. N.: Radium isotopes as tracers of iron sources fueling a Southern Ocean
710 phytoplankton bloom, Deep Sea Research Part II: Topical Studies in Oceanography, 54, 1989-
711 1998, <https://doi.org/10.1016/j.dsr2.2007.06.003>, 2007.

712 Chen, J., Edwards, R. L., and Wasserburg, G. J.: ^{238}U , ^{234}U and ^{232}Th in seawater, Earth and
713 Planetary Science Letters, 80, 241-251, [https://doi.org/10.1016/0012-821X\(86\)90108-1](https://doi.org/10.1016/0012-821X(86)90108-1), 1986.

714 Coale, K. H., and Bruland, K. W.: ^{234}Th : ^{238}U disequilibria within the California Current 1,
715 *Limnology and Oceanography*, 30, 22-33, <https://doi.org/10.4319/lo.1985.30.1.0022>, 1985.

716 Coale, K. H., and Bruland, K. W.: Oceanic stratified euphotic zone as elucidated by ^{234}Th :
717 ^{238}U disequilibria 1, *Limnology and Oceanography*, 32, 189-200,
718 <https://doi.org/10.4319/lo.1987.32.1.0189>, 1987.

719 Cochran, J., and Masqué, P.: Short-lived U/Th series radionuclides in the ocean: tracers for
720 scavenging rates, export fluxes and particle dynamics, *Reviews in Mineralogy and*
721 *geochemistry*, 52, 461-492, <https://doi.org/10.2113/0520461>, 2003.

722 Dengler, M., and Sommer, S.: Coupled benthic and pelagic oxygen, nutrient and trace metal
723 cycling, ventilation and carbon degradation in the oxygen minimum zone of the Peruvian
724 continental margin (SFB 754): Cruise No. M 136 11.04.–03.05. 2017 Callao (Peru)–Callao
725 Solute-Flux Peru I, *METEOR-Berichte*, 10.3289/CR_M136, 2017, 2017.

726 Dunne, J. P., and Murray, J. W.: Sensitivity of ^{234}Th export to physical processes in the
727 central equatorial Pacific, *Deep Sea Research Part I: Oceanographic Research Papers*, 46,
728 831-854, [https://doi.org/10.1016/S0967-0637\(98\)00098-3](https://doi.org/10.1016/S0967-0637(98)00098-3), 1999.

729 Echevin, V. M., Colas, F., Espinoza-Morriberon, D., Anculle, T., Vasquez, L., and Gutierrez,
730 D.: Forcings and evolution of the 2017 coastal El Niño off Northern Peru and Ecuador,
731 *Frontiers in Marine Science*, 5, 367, <https://doi.org/10.3389/fmars.2018.00367>, 2018.

732 Fischer, J., Brandt, P., Dengler, M., Müller, M., and Symonds, D.: Surveying the upper ocean
733 with the Ocean Surveyor: a new phased array Doppler current profiler, *Journal of*
734 *Atmospheric and Oceanic Technology*, 20, 742-751, [https://doi.org/10.1175/1520-0426\(2003\)20<742:STUOWT>2.0.CO;2](https://doi.org/10.1175/1520-0426(2003)20<742:STUOWT>2.0.CO;2), 2003.

736 Garreaud, R. D.: A plausible atmospheric trigger for the 2017 coastal El Niño, *International*
737 *Journal of Climatology*, 38, e1296-e1302, <https://doi.org/10.1002/joc.5426>, 2018.

738 Gregg, M., D'Asaro, E., Riley, J., and Kunze, E.: Mixing efficiency in the ocean, *Annual*
739 *review of marine science*, 10, 443-473, [10.1146/annurev-marine-121916-063643](https://doi.org/10.1146/annurev-marine-121916-063643), 2018.

740 Gustafsson, Ö., Buesseler, K. O., Rockwell Geyer, W., Bradley Moran, S., and Gschwend, P.
741 M.: An assessment of the relative importance of horizontal and vertical transport of particle-
742 reactive chemicals in the coastal ocean, *Continental Shelf Research*, 18, 805-829,
743 [https://doi.org/10.1016/S0278-4343\(98\)00015-6](https://doi.org/10.1016/S0278-4343(98)00015-6), 1998.

744 Hahn, J., Brandt, P., Greatbatch, R. J., Krahnemann, G., and Körtzinger, A.: Oxygen variance
745 and meridional oxygen supply in the Tropical North East Atlantic oxygen minimum zone,
746 *Climate dynamics*, 43, 2999-3024, <https://doi.org/10.1007/s00382-014-2065-0>, 2014.

747 Henson, S. A., Sanders, R., Madsen, E., Morris, P. J., Le Moigne, F., and Quartly, G. D.: A
748 reduced estimate of the strength of the ocean's biological carbon pump, *Geophysical Research*
749 *Letters*, 38, 10.1029/2011gl046735, 2011.

750 Kadko, D.: Upwelling and primary production during the US GEOTRACES East Pacific
751 Zonal Transect, *Global Biogeochemical Cycles*, 31, 218-232,
752 <https://doi.org/10.1002/2016GB005554>, 2017.

753 Kaufman, A., Li, Y.-H., and Turekian, K. K.: The removal rates of ^{234}Th and ^{228}Th from
754 waters of the New York Bight, *Earth and Planetary Science Letters*, 54, 385-392,
755 [https://doi.org/10.1016/0012-821X\(81\)90054-6](https://doi.org/10.1016/0012-821X(81)90054-6), 1981.

756 Keeling, R. F., and Garcia, H. E.: The change in oceanic O_2 inventory associated with recent
757 global warming, *Proceedings of the National Academy of Sciences*, 99, 7848-7853,
758 10.1073/pnas.122154899, 2002.

759 Kim, G., Hussain, N., and Church, T. M.: How accurate are the ^{234}Th based particulate
760 residence times in the ocean?, *Geophysical research letters*, 26, 619-622,
761 <https://doi.org/10.1029/1999GL900037>, 1999.

762 Ku, T.-L., Knauss, K. G., and Mathieu, G. G.: Uranium in open ocean: concentration and
763 isotopic composition, *Deep Sea Research*, 24, 1005-1017, [https://doi.org/10.1016/0146-](https://doi.org/10.1016/0146-6291(77)90571-9)
764 [6291\(77\)90571-9](https://doi.org/10.1016/0146-6291(77)90571-9), 1977.

765 Law, C., Martin, A., Liddicoat, M., Watson, A., Richards, K., and Woodward, E.: A
766 Lagrangian SF₆ tracer study of an anticyclonic eddy in the North Atlantic: Patch evolution,
767 vertical mixing and nutrient supply to the mixed layer, *Deep Sea Research Part II: Topical
768 Studies in Oceanography*, 48, 705-724, [https://doi.org/10.1016/S0967-0645\(00\)00112-0](https://doi.org/10.1016/S0967-0645(00)00112-0),
769 2001.

770 Le Moigne, F. A. C., Henson, S. A., Sanders, R. J., and Madsen, E.: Global database of
771 surface ocean particulate organic carbon export fluxes diagnosed from the ²³⁴Th technique,
772 *Earth Syst. Sci. Data*, 5, 295-304, <https://doi.org/10.5194/essd-5-295-2013>, 2013.

773 Lee, C., Murray, D., Barber, R., Buesseler, K., Dymond, J., Hedges, J., Honjo, S., Manganini,
774 S., Marra, J., and Moser, C.: Particulate organic carbon fluxes: compilation of results from the
775 1995 US JGOFS Arabian Sea process study: By the Arabian Sea carbon flux group, *Deep Sea
776 Research Part II: Topical Studies in Oceanography*, 45, 2489-2501,
777 [https://doi.org/10.1016/S0967-0645\(98\)00079-4](https://doi.org/10.1016/S0967-0645(98)00079-4), 1998.

778 Lüdke, J., Dengler, M., Sommer, S., Clemens, D., Thomsen, S., Krahnemann, G., Dale, A. W.,
779 Achterberg, E. P., and Visbeck, M.: Influence of intraseasonal eastern boundary circulation
780 variability on hydrography and biogeochemistry off Peru, *Ocean Sci. Discuss.*, 2019, 1-31,
781 <https://doi.org/10.5194/os-2019-93>, in review 2020.

782 McKee, B. A., DeMaster, D. J., and Nittrouer, C. A.: Uranium geochemistry on the Amazon
783 shelf: Evidence for uranium release from bottom sediments, *Geochimica et Cosmochimica
784 Acta*, 51, 2779-2786, [https://doi.org/10.1016/0016-7037\(87\)90157-8](https://doi.org/10.1016/0016-7037(87)90157-8), 1987.

785 Morris, P. J., Sanders, R., Turnewitsch, R., and Thomalla, S.: ²³⁴Th-derived particulate
786 organic carbon export from an island-induced phytoplankton bloom in the Southern Ocean,
787 *Deep Sea Research Part II: Topical Studies in Oceanography*, 54, 2208-2232,
788 <https://doi.org/10.1016/j.dsr2.2007.06.002>, 2007.

789 Murray, J. W., Downs, J. N., Strom, S., Wei, C.-L., and Jannasch, H. W.: Nutrient
790 assimilation, export production and ²³⁴Th scavenging in the eastern equatorial Pacific, *Deep*

791 Sea Research Part A. Oceanographic Research Papers, 36, 1471-1489,
792 [https://doi.org/10.1016/0198-0149\(89\)90052-6](https://doi.org/10.1016/0198-0149(89)90052-6), 1989.

793 Nameroff, T., Balistrieri, L., and Murray, J.: Suboxic trace metal geochemistry in the eastern
794 tropical North Pacific, *Geochimica et Cosmochimica Acta*, 66, 1139-1158,
795 [https://doi.org/10.1016/S0016-7037\(01\)00843-2](https://doi.org/10.1016/S0016-7037(01)00843-2), 2002.

796 Noffke, A., Hensen, C., Sommer, S., Scholz, F., Bohlen, L., Mosch, T., Graco, M., and
797 Wallmann, K.: Benthic iron and phosphorus fluxes across the Peruvian oxygen minimum
798 zone, *Limnology and Oceanography*, 57, 851-867, <https://doi.org/10.4319/lo.2012.57.3.0851>,
799 2012.

800 Osborn, T.: Estimates of the local rate of vertical diffusion from dissipation measurements,
801 *Journal of physical oceanography*, 10, 83-89, [https://doi.org/10.1175/1520-0485\(1980\)010<0083:EOTLRO>2.0.CO;2](https://doi.org/10.1175/1520-0485(1980)010<0083:EOTLRO>2.0.CO;2), 1980.

803 Owens, S., Buesseler, K., and Sims, K.: Re-evaluating the ^{238}U -salinity relationship in
804 seawater: Implications for the ^{238}U - ^{234}Th disequilibrium method, *Marine Chemistry*, 127, 31-
805 39, <https://doi.org/10.1016/j.marchem.2011.07.005>, 2011.

806 Owens, S. A., Pike, S., and Buesseler, K. O.: Thorium-234 as a tracer of particle dynamics
807 and upper ocean export in the Atlantic Ocean, *Deep Sea Research Part II: Topical Studies in*
808 *Oceanography*, 116, 42-59, <http://dx.doi.org/10.1016/j.dsr2.2014.11.010>, 2015.

809 Peng, Q., Xie, S.-P., Wang, D., Zheng, X.-T., and Zhang, H.: Coupled ocean-atmosphere
810 dynamics of the 2017 extreme coastal El Niño, *Nature Communications*, 10, 298,
811 [10.1038/s41467-018-08258-8](https://doi.org/10.1038/s41467-018-08258-8), 2019.

812 Pike, S., Buesseler, K., Andrews, J., and Savoye, N.: Quantification of ^{234}Th recovery in small
813 volume sea water samples by inductively coupled plasma-mass spectrometry, *Journal of*
814 *Radioanalytical and Nuclear Chemistry*, 263, 355-360, <https://doi.org/10.1007/s10967-005-0594-z>, 2005.

816 Puigcorbé, V., Masqué, P., and Le Moigne, F. A. C.: Global database of ratios of particulate
817 organic carbon to thorium-234 in the ocean: improving estimates of the biological carbon
818 pump, *Earth Syst. Sci. Data*, 12, 1267-1285, 10.5194/essd-12-1267-2020, 2020.

819 Rapp, I., Schlosser, C., Menzel Barraqueta, J. L., Wenzel, B., Lüdke, J., Scholten, J., Gasser,
820 B., Reichert, P., Gledhill, M., Dengler, M., and Achterberg, E. P.: Controls on redox-sensitive
821 trace metals in the Mauritanian oxygen minimum zone, *Biogeosciences*, 16, 4157-4182,
822 10.5194/bg-16-4157-2019, 2019.

823 Rengarajan, R., Sarin, M., and Krishnaswami, S.: Uranium in the Arabian Sea: role of
824 denitrification in controlling its distribution, *Oceanologica acta*, 26, 687-693,
825 <https://doi.org/10.1016/j.oceact.2003.05.001>, 2003.

826 Resplandy, L., Martin, A. P., Le Moigne, F., Martin, P., Aquilina, A., Mémery, L., Lévy, M.,
827 and Sanders, R.: How does dynamical spatial variability impact ²³⁴Th-derived estimates of
828 organic export?, *Deep Sea Research Part I: Oceanographic Research Papers*, 68, 24-45,
829 <https://doi.org/10.1016/j.dsr.2012.05.015>, 2012.

830 Rosengard, S. Z., Lam, P. J., Balch, W. M., Auro, M. E., Pike, S., Drapeau, D., and Bowler,
831 B.: Carbon export and transfer to depth across the Southern Ocean Great Calcite Belt,
832 doi:10.5194/bg-12-3953-2015, 2015.

833 Santschi, P., Murray, J. W., Baskaran, M., Benitez-Nelson, C. R., Guo, L., Hung, C.-C.,
834 Lamborg, C., Moran, S., Passow, U., and Roy-Barman, M.: Thorium speciation in seawater,
835 *Marine Chemistry*, 100, 250-268, 2006.

836 Savoye, N., Benitez-Nelson, C., Burd, A. B., Cochran, J. K., Charette, M., Buesseler, K. O.,
837 Jackson, G. A., Roy-Barman, M., Schmidt, S., and Elskens, M.: ²³⁴Th sorption and export
838 models in the water column: a review, *Marine Chemistry*, 100, 234-249,
839 <https://doi.org/10.1016/j.marchem.2005.10.014>, 2006.

840 Schafstall, J., Dengler, M., Brandt, P., and Bange, H.: Tidal - induced mixing and diapycnal
841 nutrient fluxes in the Mauritanian upwelling region, *Journal of Geophysical Research:*
842 *Oceans*, 115, <https://doi.org/10.1029/2009jc005940>, 2010, 2010.

843 Schmidt, S., and Reyss, J.: Uranium concentrations of Mediterranean seawater with high
844 salinities, *Comptes Rendus de l'Academie des Sciences. Serie 2*, 312, 479-484, 1991.

845 Schmidtko, S., Stramma, L., and Visbeck, M.: Decline in global oceanic oxygen content
846 during the past five decades, *Nature*, 542, 335, [10.1038/nature21399](https://doi.org/10.1038/nature21399), 2017.

847 Scholz, F., Hensen, C., Noffke, A., Rohde, A., Liebetrau, V., and Wallmann, K.: Early
848 diagenesis of redox-sensitive trace metals in the Peru upwelling area—response to ENSO-
849 related oxygen fluctuations in the water column, *Geochimica et Cosmochimica Acta*, 75,
850 7257-7276, [10.1016/j.gca.2011.08.007](https://doi.org/10.1016/j.gca.2011.08.007), 2011.

851 Scholz, F., McManus, J., Mix, A. C., Hensen, C., and Schneider, R. R.: The impact of ocean
852 deoxygenation on iron release from continental margin sediments, *Nature Geosci*, 7, 433-437,
853 <https://doi.org/10.1038/ngeo2162>, 2014.

854 Shepherd, J. G., Brewer, P. G., Oschlies, A., and Watson, A. J.: Ocean ventilation and
855 deoxygenation in a warming world: introduction and overview, *Philosophical Transactions of*
856 *the Royal Society A: Mathematical, Physical and Engineering Sciences*, 375, 20170240,
857 [doi:10.1098/rsta.2017.0240](https://doi.org/10.1098/rsta.2017.0240), 2017.

858 Smith, S. D.: Coefficients for sea surface wind stress, heat flux, and wind profiles as a
859 function of wind speed and temperature, *Journal of Geophysical Research: Oceans*, 93,
860 15467-15472, <https://doi.org/10.1029/JC093iC12p15467>, 1988.

861 Steinfeldt, R., Sültenfuß, J., Dengler, M., Fischer, T., and Rhein, M.: Coastal upwelling off
862 Peru and Mauritania inferred from helium isotope disequilibrium, *Biogeosciences*, 12, 7519-
863 7533, <https://doi.org/10.5194/bg-12-7519-2015>, 2015.

864 Stramma, L., Johnson, G. C., Sprintall, J., and Mohrholz, V.: Expanding oxygen-minimum
865 zones in the tropical oceans, *science*, 320, 655-658, 2008.

866 Suess, E., Kulm, L., and Killingley, J.: Coastal upwelling and a history of organic-rich
867 mudstone deposition off Peru, Geological Society, London, Special Publications, 26, 181-197,
868 1987.

869 Swarzenski, P., Campbell, P., Porcelli, D., and McKee, B.: The estuarine chemistry and
870 isotope systematics of $^{234,238}\text{U}$ in the Amazon and Fly Rivers, Continental Shelf Research, 24,
871 2357-2372, <https://doi.org/10.1016/j.csr.2004.07.025>, 2004.

872 Thomsen, S., Kanzow, T., Krahnmann, G., Greatbatch, R. J., Dengler, M., and Lavik, G.: The
873 formation of a subsurface anticyclonic eddy in the Peru - Chile Undercurrent and its impact
874 on the near - coastal salinity, oxygen, and nutrient distributions, Journal of Geophysical
875 Research: Oceans, 121, 476-501, <https://doi.org/10.1002/2015JC010878>, 2016.

876 Van Der Loeff, M. R., Sarin, M. M., Baskaran, M., Benitez-Nelson, C., Buesseler, K. O.,
877 Charette, M., Dai, M., Gustafsson, Ö., Masque, P., and Morris, P. J.: A review of present
878 techniques and methodological advances in analyzing ^{234}Th in aquatic systems, Marine
879 Chemistry, 100, 190-212, <https://doi.org/10.1016/j.marchem.2005.10.012>, 2006.

880 Waples, J. T., Benitez-Nelson, C., Savoye, N., van der Loeff, M. R., Baskaran, M., and
881 Gustafsson, Ö.: An introduction to the application and future use of ^{234}Th in aquatic systems,
882 Marine Chemistry, 100, 166-189, <https://doi.org/10.1016/j.marchem.2005.10.011>, 2006.

883 Weinstein, S. E., and Moran, S. B.: Vertical flux of particulate Al, Fe, Pb, and Ba from the
884 upper ocean estimated from $^{234}\text{Th}/^{238}\text{U}$ disequilibria, Deep Sea Research Part I:
885 Oceanographic Research Papers, 52, 1477-1488, <https://doi.org/10.1016/j.dsr.2005.03.008>,
886 2005.

887 Zhurbas, V., and Oh, I. S.: Drifter - derived maps of lateral diffusivity in the Pacific and
888 Atlantic oceans in relation to surface circulation patterns, Journal of Geophysical Research:
889 Oceans, 109, <https://doi.org/10.1029/2003JC002241>, 2004.

890 Zimmerman, J. T. F.: Mixing and flushing of tidal embayments in the western Dutch Wadden
891 Sea part I: Distribution of salinity and calculation of mixing time scales, Netherlands Journal
892 of Sea Research, 10, 149-191, 1976.

893

894

895 Figure captions

896 Figure 1. Maps showing (a) locations of each station from M136 (white squares) and M138
897 (grey circles) and (B) monthly-averaged current field in the top 15 m from April 16 to May
898 15, 2017 derived from altimetry measurements (<http://marine.copernicus.eu/>; product ID:
899 MULTI OBS_GLO-PHY_REP_015_004). Color boxes in (a) schematically divide the four
900 shelf-offshore transects. Map (a) was created with Ocean Data View (Schlitzer, 2014). The
901 white box in (b) highlights our study area.

902

903 Figure 2. Profiles of ^{238}U (black) and ^{234}Th (orange squares – M136; orange circles – M138)
904 along with concentrations of oxygen (grey) and fluorescence (green). Profiles are organized
905 by cruises, transects, and distance to shore from left to right and top to bottom, indicated by
906 east (E) to west (W) arrows. Error bars for both ^{238}U and ^{234}Th are indicated. Red dashed lines
907 indicate the depth of the mixed layer. The start of the oxygen deficient zone is where oxygen
908 diminishes. Bottom depths are indicated for stations whose bottom depths are shallower than
909 600 m.

910

911 Figure 3. Shelf-offshore distributions of $^{234}\text{Th}/^{238}\text{U}$ along the four studied transects, as shown
912 in Figure 1, for M136 (left) and M138 (right). White dots denote station location.

913

914 Figure 4. Distributions of averaged ^{234}Th activities during M136 (a, top 30 m) and M138 (b,
915 top 50 m).

916

917 Figure 5. Profiles of temperature (solid lines) and salinity (dashed lines) for (a) repeated
918 stations 458 (purple) and 508 (yellow), and (d) 495 (blue) and 516 (orange); (b) and (c)
919 respectively profiles for stations 458 and 508 of ^{238}U (black), ^{234}Th (color squares), and
920 concentrations of oxygen (grey) and fluorescence (green). (e) and (f) respectively profiles for
921 stations 495 and 516 of ^{238}U (black), ^{234}Th (color squares), and concentrations of oxygen
922 (grey) and fluorescence (green).

923

924 Figure 6. Bar charts of ^{234}Th fluxes due to production and decay (blue), upwelling (orange),
925 and vertical diffusion (grey) for the depths at 5 – 20 m below the ML (top) and 100 m
926 (bottom). Color boxes corresponds to individual transects in Figure 1. Within each transect
927 stations from west (offshore) to east (nearshore) are listed from left to right. Error bars (1SE)
928 are indicated.

929

930 Figure 7. Cross plots of measured ^{238}U activities vs. salinity for M136 (a) and M138 (b),
931 showing poor linear relationship between ^{238}U and salinity. (c) shows a direct comparison
932 between measured and salinity-based ^{238}U to further highlight the large difference between the
933 two. The solid blue line indicates the 1:1 ratio between measured and projected ^{238}U . Blue
934 dashed lines indicate the \pm errors reported in Owens et al. (2011).

Table 1. ²³⁴Th fluxes due to production and decay, upwelling and vertical diffusion below the mixed layer and at 100 m. Horizontal advective fluxes were not quantified at 100 m. Refer to text for details.

Cruise	Station	Mixed layer			Maximum fluorescence	Equilibrium depth	²³⁴ Th flux at the base of the ML						²³⁴ Th flux at 100 m						
		Cast depth	oxycline depth	depth			Depth	Production and decay	Upwelling	Diffusion	Final flux	1 SD	Production and decay	Upwelling	Diffusion	Final flux	1 SD		
		m	m	m	µg L ⁻¹	m	m	dpm m ⁻² d ⁻¹	dpm m ⁻² d ⁻¹	dpm m ⁻² d ⁻¹	dpm m ⁻² d ⁻¹	dpm m ⁻² d ⁻¹	dpm m ⁻² d ⁻¹	dpm m ⁻² d ⁻¹	dpm m ⁻² d ⁻¹	dpm m ⁻² d ⁻¹	dpm m ⁻² d ⁻¹	dpm m ⁻² d ⁻¹	dpm m ⁻² d ⁻¹
M136	353	1	25	102	1.20	100	30	907	52	-36	923	69	1422	-14	2	1410	189		
M136	380	1	26	129	0.87	80	30	1145	0	-41	1105	54	1637	0	-1	1637	132		
M136	402	1	24	129	7.51	100	30	808	0	-75	732	64	1234	0	2	1236	111		
M136	428	1	10	76	4.11	30	30	983	-128	493	1348	129	1772	33	-390	1415	256		
M136	445	1	17	64	2.07	100	30	820	-10	16	826	66	1621	53	6	1681	165		
M136	458	1	5	55	1.61	100	30	1012	-18	161	1155	117	2101	-11	145	2235	238		
M136	472	1	11	29	7.41	200	40	1887	15	-29	1872	77	3315	-12	63	3366	233		
M136	495	1	18	50	1.13	200	30	1149	1	-19	1130	50	3195	2	-5	3192	89		
M136	516	1	16	45	3.77	200	30	614	0	1	615	49	2229	2	-4	2227	109		
M136	547	1	22	48	1.28	150	30	791	0	85	877	61	2510	0	-15	2495	118		
M136	559	1	20	79	1.70	85	50	623	3	-67	559	117	854	-4	2	852	120		
M136	567	1	21	50	2.40	150	30	1593	0	-23	1570	52	3011	0	-11	3000	86		
M138	879	3	43	93	2.24	200	60	1249	0	-16	1266	91	1702	0	-5	1697	111		
M138	882	10	39	211	2.68	150	50	1321	-7	16	1331	63	2264	19	-12	2272	82		
M138	883	12	10	220	1.31	250	30	683	-84	-159	758	108	1782	31	-121	1692	179		
M138	888	7	41	127	1.59	150	50	1364	0	-120	1244	62	1813	0	-4	1809	86		
M138	892	14	47	128	1.05	100	60	1395	33	-118	1309	72	1743	-3	1	1741	99		
M138	898	1	38	101	1.42	60	50	1099	0	-19	1080	104	1091	0	0	1091	125		
M138	904	16	12	72	3.63	150	20	812	275	0	1087	76	2643	0	-9	2634	79		
M138	906	18	32	81	1.73	200	40	1796	0	4	1799	41	3100	0	-1	3100	77		
M138	907	11	31	100	1.29	60	60	1594	-88	13	1518	147	1787	67	-2	1853	140		
M138	912	3	37	70	2.75	>600	50	1960	0	-79	1881	43	2975	0	-3	2972	78		
M138	915	1	26	99	3.51	200	40	1628	0	22	1650	38	2752	0	0	2752	93		
M138	919	1	19	79	4.46	150	30	1316	0	49	1365	32	3249	0	-8	3241	85		

Table 2. Comparison of ^{234}Th fluxes at 100 m calculated with measured ^{238}U activities and those with salinity-based ^{238}U .

Cruise	Station	Cast	^{234}Th fluxes at 100 m*		Difference %
			measured $\text{dpm m}^{-2} \text{d}^{-1}$	predicted $\text{dpm m}^{-2} \text{d}^{-1}$	
M136	353	1	1422	1320	8
M136	380	1	1637	1304	26
M136	402	1	1234	865	43
M136	428	1	1772	1443	23
M136	445	1	1621	1365	19
M136	458	1	2101	1859	13
M136	472	1	3315	3073	8
M136	495	1	3195	3058	4
M136	516	1	2229	2140	4
M136	547	1	2510	2313	9
M136	559	1	854	751	14
M136	567	1	3011	2879	5
M138	879	3	1702	1515	12
M138	882	10	2264	1875	21
M138	883	12	1782	1352	32
M138	888	7	1813	1441	26
M138	892	14	1743	1257	39
M138	898	1	1091	770	42
M138	904	16	2643	2280	16
M138	906	18	3100	2673	16
M138	907	11	1787	1308	37
M138	912	3	2975	2572	16
M138	915	1	2752	2380	16
M138	919	1	3249	2862	14

* For comparison purposes, we only report here ^{234}Th fluxes due to radioactive production and decay.

Table 3. Residence time of total ^{234}Th in the surface layers of Peruvian OMZ.

Cruise	Station	Cast	Average ^{234}Th in	Residence time
			the surface layer* dpm L ⁻¹	days
M136	353	1	1.48	46
M136	380	1	1.35	35
M136	402	1	1.64	61
M136	428	1	1.57	35
M136	445	1	1.64	61
M136	458	1	1.45	38
M136	472	1	0.93	20
M136	495	1	1.20	31
M136	516	1	1.74	85
M136	547	1	1.67	63
M136	559	1	1.75	94
M136	567	1	1.41	45
M138	879	3	1.59	75
M138	882	10	1.81	69
M138	883	12	1.87	74
M138	888	7	1.68	67
M138	892	14	1.69	65
M138	898	1	1.66	92
M138	904	16	1.32	24
M138	906	18	1.15	25
M138	907	11	1.04	41
M138	912	3	1.25	33
M138	915	1	1.16	28
M138	919	1	1.17	26

* Here 'surface layer' refers to the top 30 m during M136 and top 50 m during M138.

Figure 1

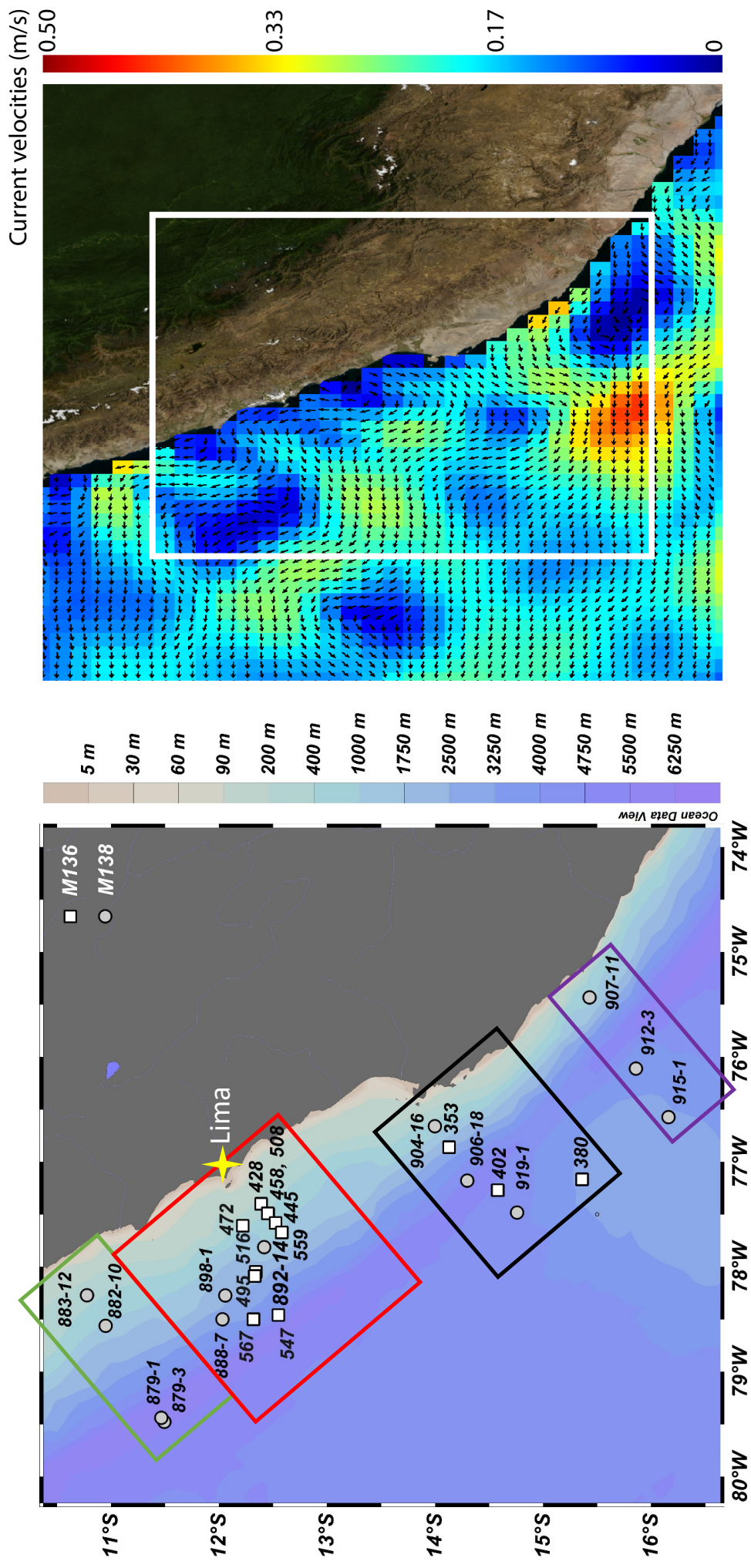
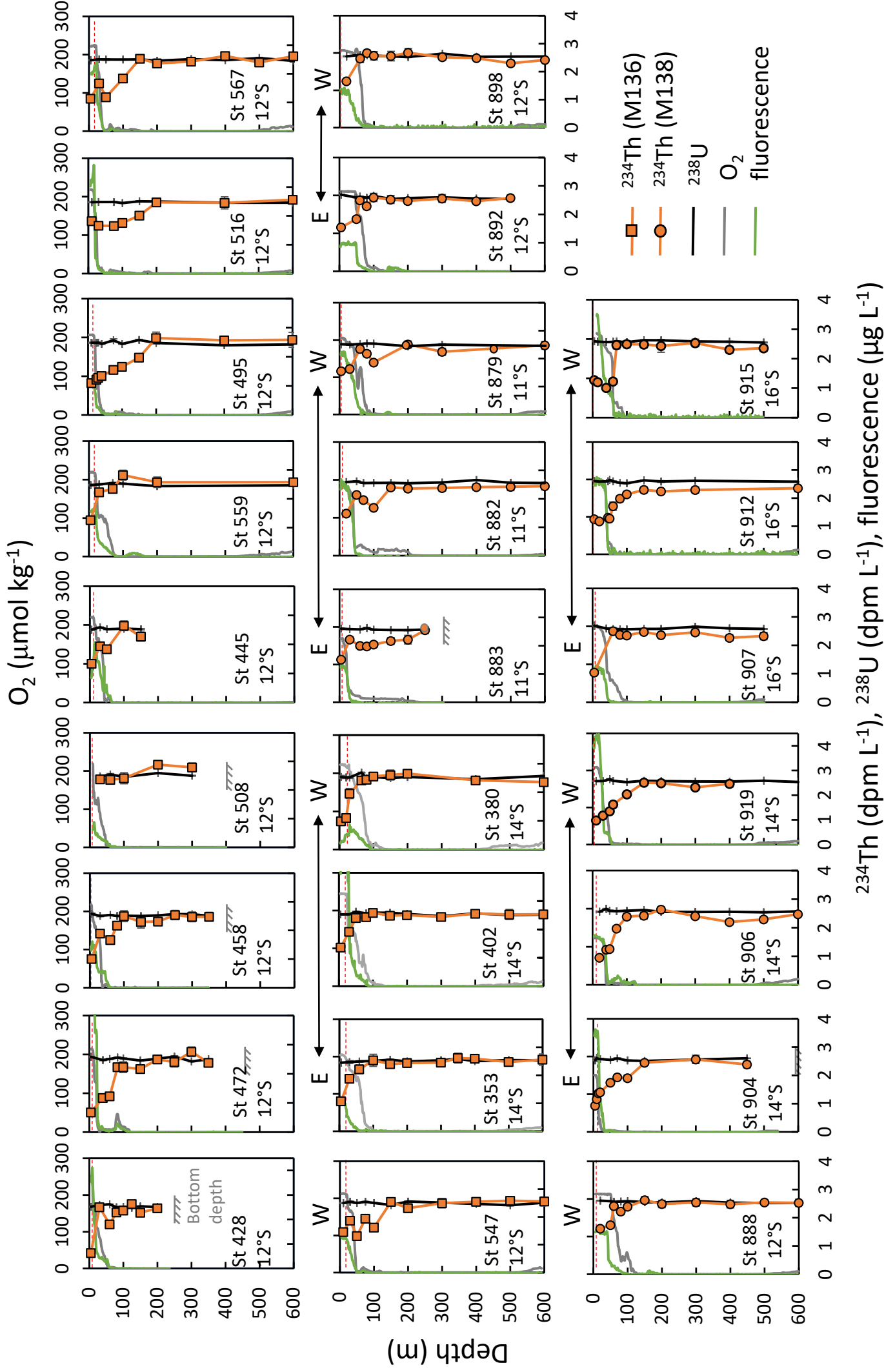


Figure 2

E ← → W



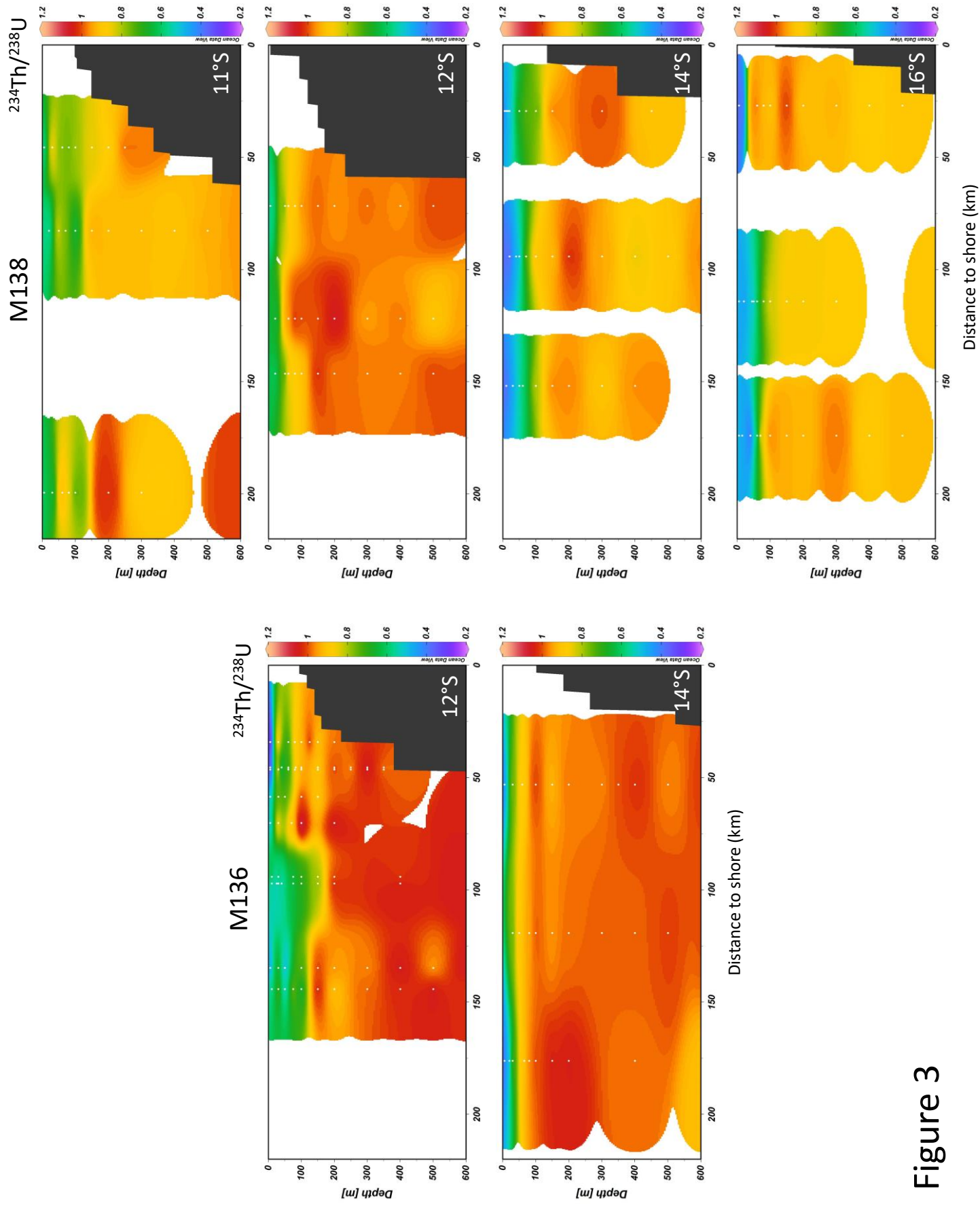


Figure 3

Figure 4

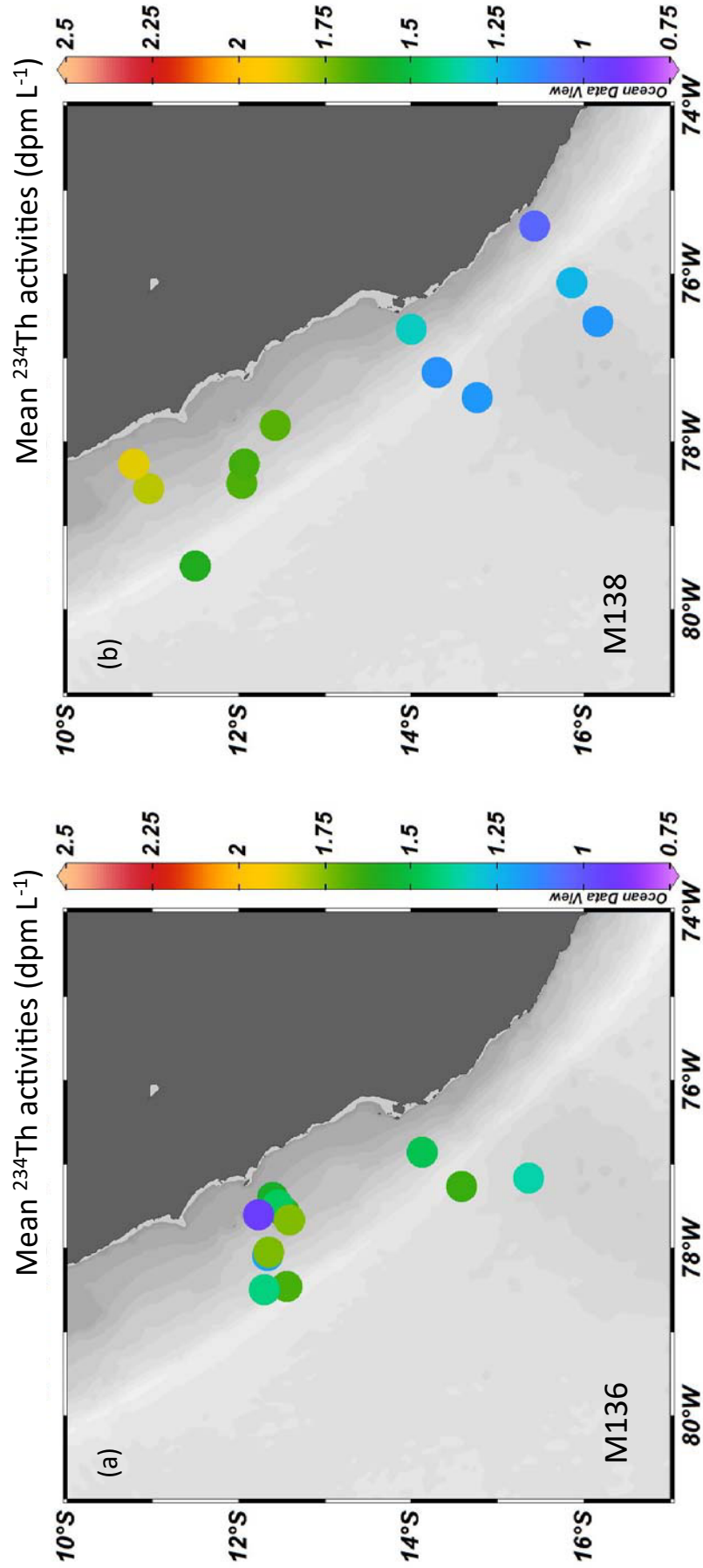


Figure 5

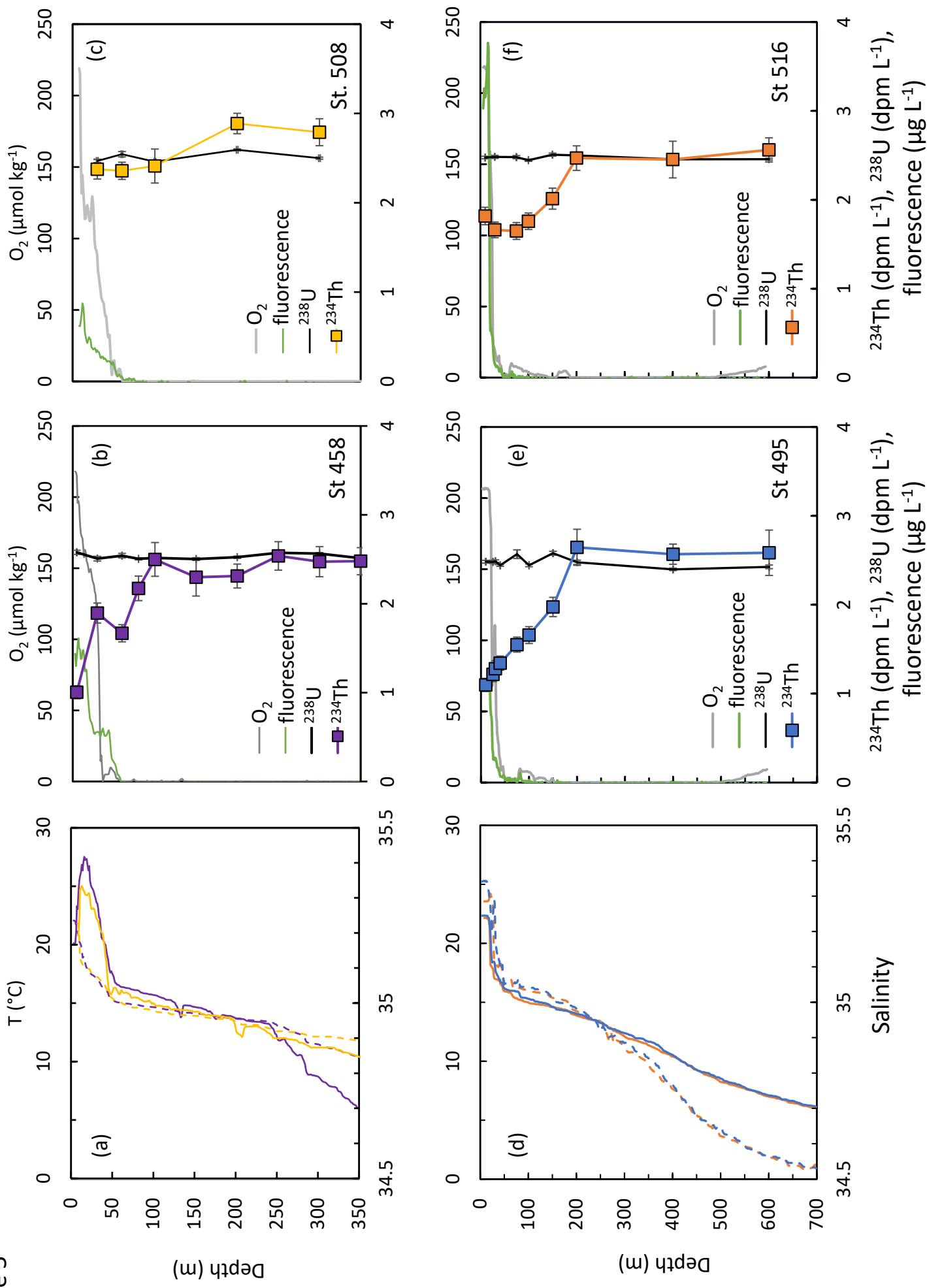


Figure 6

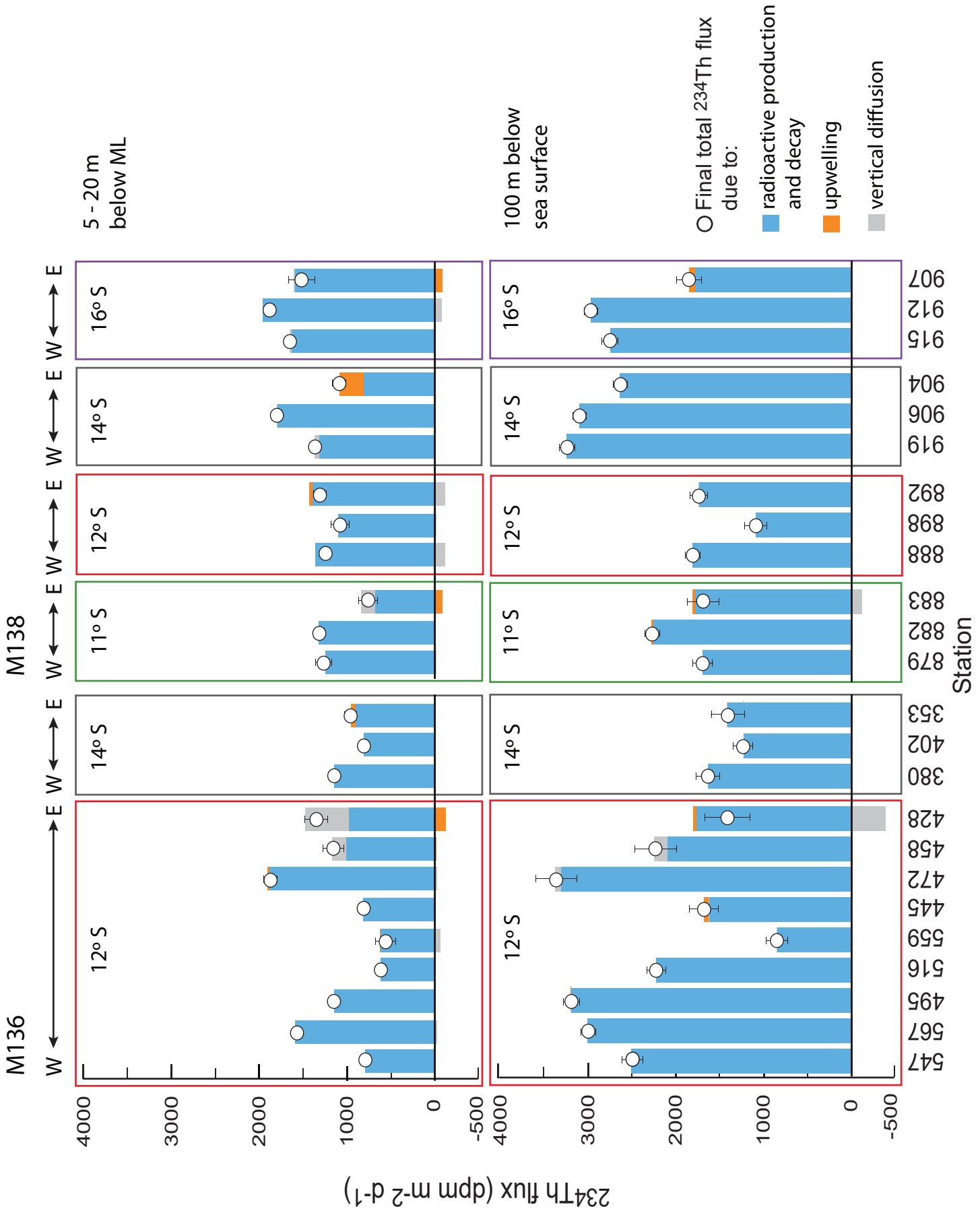


Figure 7

